

Versión Definitiva. Incluye cambios sugeridos por revisores.



18-01-2021



CENTRO DE INVESTIGACIONES  
EN OPTICA, A.C.

# “PHOTONIC CRYSTAL NANOBEAM CAVITIES FOR 2D EMITTERS”



Tesis para obtener el grado de Maestro en Ciencias (Óptica)

***Presenta: Oscar Camacho Ibarra***

*Director de Tesis: Dr. Roberto Ramírez Alarcón*

*León · Guanajuato · México*

*Enero de 2021*



## Acknowledgments

First and foremost, I would like to thank my parents Oscar Camacho García and Martha Silvia Ibarra Euresty, for all their constant support they have been giving me from the beginning of my professional career.

I am very thankful to my supervisor Dr. Roberto Ramírez Alarcón for his guidance and support through the whole project. You were very helpful and kind.

I want to thank Prof. Val Zwiller and Prof. Klaus Jöns for giving me the opportunity of doing my internship in their research group. The skills I learned during this internship will be extremely valuable in the future.

I want to thank Dr. Artur Branny for his valuable feedback and support throughout this project.

I also want to thank Samuel Gyger for his help and guidance with the fabrication of the samples in this project.

I want to thank CONACYT for the scholarship they granted me, without it this work would have not been possible.

Finally, I would also like to thank my girlfriend Joanne Shen for all her encouragement and unwavering support through the whole development of the present work.

## Abstract

In the area of photonics, photonic crystals are of great interest since they possess photonic band gaps. Therefore, the crystals are also known as photonic band gap materials. The photonic band gaps of these materials are the key property which enables the design and fabrication of devices capable of controlling light propagation and light confinement: mirrors, waveguides, cavities, filters, and optical isolators. Furthermore, the manipulation of light that photonic crystals grant, can also be exploited in other areas of research such as: chemical sensing, biomedics, gas sensing, solar cells and communications. Among the devices previously mentioned, photonic crystal nanobeam cavities have proven to be the best resonator choice for integrated optics. Since these cavities are capable of providing large Purcell factors, thanks to their achievable high-quality factors (Q) and small mode volumes. For the purpose of latter integration with single photons emitters, in the present work a 1-D deterministic photonic crystal nanocavity design, with high in-line coupling to a waveguide, is investigated and used to fabricate two nanobeam cavities on a  $Si_3N_4 - on - SiO_2$  platform for two different operational wavelengths: 890 nm and 646 nm. The photonic crystal nanobeam cavities were optimized through finite difference time domain (FDTD) simulations and later were fabricated via combination of electron beam lithography and dry etching technology. The cavities fabricated in this work exhibited quality factors on the range of 1000 to 10000 and mode volumes as small as  $0.63\left(\frac{\lambda_c}{n_{Si_3N_4}}\right)^3$  and  $0.94\left(\frac{\lambda_c}{n_{Si_3N_4}}\right)^3$ .

# Index

Acknowledgments .....	i
Abstract .....	ii
List of Figures .....	v
Introduction.....	1
<b>Chapter 1 Theory.....</b>	<b>3</b>
1.1 Maxwell's equations and the Eigenvalue problem .....	3
1.1.1 Scaling property .....	6
1.1.2 An important characteristic of the modes H.....	7
1.2 Photonic crystals.....	8
1.2.1 The origin of the photonic band gap .....	13
1.2.2 Defects and cavities .....	15
<b>Chapter 2 Modelling of photonic structures .....</b>	<b>18</b>
2.1 Lumerical FDTD.....	18
2.1.1 Mesh size .....	20
2.1.2 Boundary conditions.....	21
2.1.3 Q-factor calculation .....	22
<b>Chapter 3 Fabrication .....</b>	<b>24</b>
3.1 $Si_3N_4$ -on- $SiO_2$ platform .....	25
3.2 Cleaving.....	25
3.3 Cleaning and Spin-coating.....	26
3.4 Lithography and Development .....	28
3.5 Etching.....	29

3.6 The Design .....	32
<b>Chapter 4 Results</b> .....	<b>35</b>
4.1 Simulations .....	35
4.2 Characterization of the fabricated cavities .....	41
4.2.1 Cavity operating at 646 nm .....	42
4.2.1 Cavity operating at 890 nm .....	46
4.3 Discussion and further work.....	51
Conclusions.....	54
Bibliography.....	56

# List of Figures

<b>Fig. 1 Photonic crystals periodic in one, two, and three dimensions.....</b>	<b>9</b>
<b>Fig. 2 Dielectric configuration in one dimension. The lattice constant is indicated. ....</b>	<b>10</b>
<b>Fig. 3 Example of mode frequencies bands, the blue lines correspond to the modes localized in the dielectric. This figure was taken from [8].....</b>	<b>13</b>
<b>Fig. 4 Dispersion relation (band structure), frequency <math>\omega</math> vs wavenumber <math>k</math> of a: a) uniform medium. b) Effect on the bands of a physical periodic dielectric variation <math>\Delta\epsilon_r &gt; 0</math>. Modified from [7]. ....</b>	<b>14</b>
<b>Fig. 5 Band structure with a defect inside the photonic bandgap. Modified from [7]. ....</b>	<b>16</b>
<b>Fig. 6 1D Photonic Crystal cavity with Bragg mirror in both sides and periodicity <math>a</math>. ....</b>	<b>16</b>
<b>Fig. 7 a) Applying a big mesh step size to depict the circle, b) Applying a finer mesh to depict the circle. ....</b>	<b>20</b>
<b>Fig. 8 Circle with mesh override region, the circle has a finer mesh than its surroundings. ....</b>	<b>21</b>
<b>Fig. 9 Schematic of the main simulation components. ....</b>	<b>22</b>
<b>Fig. 10 Fourier transform of a rectangular pulse. ....</b>	<b>23</b>
<b>Fig. 11 Flow-chart showing steps of the fabrication process .....</b>	<b>24</b>
<b>Fig. 12 Schematic of <math>Si_3N_4</math>-on-<math>SiO_2</math> platform. ....</b>	<b>25</b>
<b>Fig. 13 Diagram of a crystalline solid and location of its cleavage plane .....</b>	<b>26</b>
<b>Fig. 14 Schematic of static spin coating process. ....</b>	<b>27</b>
<b>Fig. 15 Schematic of positive and negative resist after chemical developing</b>	<b>29</b>
<b>Fig. 16 Difference between anisotropic and isotropic etchings. A perfect anisotropic etching produces vertical walls, while a perfect isotropic etching removes the same amount of the targeted material in all directions. ....</b>	<b>31</b>

Fig. 17 A highly selective etching process leaves the substrate untouched (left). While a poorly selective etches the targeted layer and part of the substrate (right).....	31
Fig. 18 Oxford Plasmalab 100 etching settings and etching parameters.....	32
Fig. 19 Cavity design based on Ref. [6]. Schematic of the cavity design parameters. a) Cross-sectional view of the cavity. b) Structure seen from the top without hBN layer.....	33
Fig. 20 Schematic of a ridge-waveguide.....	35
Fig. 21 Width of a ridge waveguide for single mode operation at 646nm and 890nm. The chosen width for fabrication is shown with a dashed line...	36
Fig. 22 Dielectric and air bands at the Brillouin zone edge as function of the radius for the cavities operating at 890nm and 646nm.....	37
Fig. 23 Mirror Strength as a function of the hole radius for the cavities operating at 890nm (left hand side) and 646nm (right hand side). ....	38
Fig. 24 Full band structure of the air and dielectric bands corresponding to the first (red) and last (blue) radius of the mirror. As required, the dielectric bands of the first $r_1$ lies inside the bandgap of $r_M$ . The full band structure for the cavity operating at at 890nm is shown on the left-hand side and on the right-hand side lies the one corresponding to the cavity operating at at 646nm. ....	38
Fig. 25 Table 1: Optimal parameters of the cavities structure.....	39
Fig. 26 Mode profiles exhibiting Gaussian attenuation of $E_2$ for both cavities as function of the distance from the symmetry line of the cavity structure (see Fig. 19). The mode profile is taken at the middle plane of the cavity structure corresponding to $z=0$ . ....	40
Fig. 27 Mode profiles fitted to a Gaussian Function for both cavities as function of the distance from the symmetry line of the cavity structure. The mode profile is taken at the middle ( $y=0$ ) of the plane which is located at $z=0$ .....	40
Fig. 28 Room temperature spectroscopy setup. ....	41
Fig. 29 Fabricate cavities with scaling factor from 0.97-1.02. The green arrows at the bottom indicate the presence of more cavities with different scaling to the sides of the chip. The circle region indicates the location of the cavity. ....	43

<b>Fig. 30</b>	<b>Transmission spectra from the cavities with scaling factors from 0.95-0.99 on the upper part of the figure and on the lower part the transmission spectra for scaling factors from 1-1.05. The peak with the smallest wavelength is the mode that was designed for the operation of the cavity. A smoothing filter was applied to the data to make easier the distinction of the peaks by eye. ....</b>	<b>44</b>
<b>Fig. 31</b>	<b>Resonance wavelength as function of the scaling factor. A linear fit was performed on the data points to show the linear dependence of the resonance wavelength with the scaling factor. ....</b>	<b>45</b>
<b>Fig. 32</b>	<b>Q factors with their respective error bar for the different scaling factors. ....</b>	<b>46</b>
<b>Fig. 33</b>	<b>a) Room temperature spectroscopy setup. b) Photograph of the fabricated device with the optimal parameters of the cavity (scaling factor = 1). The circle region indicates the location of the cavity. ....</b>	<b>47</b>
<b>Fig. 34</b>	<b>SEM Image of the cavity operating at 890nm. ....</b>	<b>47</b>
<b>Fig. 35</b>	<b>Transmission spectra from the cavities with scaling factors from 0.99-1.02 on the upper part of the figure and on the lower part the transmission spectra for scaling factors from 1.03-1.06. The black arrows indicate the location of the fundamental mode. ....</b>	<b>48</b>
<b>Fig. 36</b>	<b>Resonance wavelength as function of the scaling factor. The solid line corresponds to a linear fit on the second modes of the spectrum for each scaling factor. The dashed line corresponds to a linear fit on the fundamental modes of the spectrum for the scaling factors from 1.01 to 1.06 ....</b>	<b>49</b>
<b>Fig. 37</b>	<b>Q factors with their respective error bar for the different scaling factors. The Q values of the cavities with scaling factors 0.99 and 1.00 are not from the fundamental mode, those values correspond to the Q values of the second mode. ....</b>	<b>50</b>
<b>Fig. 38</b>	<b>Transmission spectra for the sample with scaling factor of 1.04 from section 4.2.1.....</b>	<b>51</b>

# Introduction

Photonic crystals (PCs) are periodic dielectric structures that depending on the dimensionality of such periodicity, different classes of photonic crystals can be defined depending on the dimensionality of such periodicity: one-dimensional (1-D), two-dimensional (2-D) and three-dimensional (3-D) photonic crystals. These PCs possess a property known as photonic band gaps. A photonic band gap is a range of forbidden frequencies for photons to travel within the dielectric material, thus photons with energies lying in the band gap cannot propagate through the PCs [1, 2].

These photonic bandgaps can be exploited to enable the control and propagation of light inside dielectric materials [2]. Therefore, by employing PCs it is possible to fabricate devices that can shape and mold the flow of light. Some examples of these devices are mirrors, beam splitters, waveguides, cavities, filters, and optical isolators [3]. A highly promising application of PCs is to fabricate optical nanocavities that have high quality factor ( $Q$ ) and small mode volume ( $V$ ) [4, 5]. The strong light localization of these photonic crystal nanocavities can enhance light-matter interactions, and because of this they are required for various applications in the fields of optics, including quantum information processing [6, 7], optofluidics [8], optical trapping [9] and optomechanics [10].

This work focuses on the design and fabrication of these cavities, which will be later integrated with single photon emitters (SPEs) in 2D materials, which are a central building block of quantum photonics circuits. Integrating SPEs with a cavity is particularly advantageous, because it turns out that the emission rate of an emitter can be modified by changing the environment of emitter. In this case if the emitter is coupled to a cavity mode the spontaneous emission rate can be increased, and this is known as the Purcell effect. Furthermore, the coupling efficiency between the emitter and a waveguide is also increased, because the Purcell effect increases the emission rate into the cavity mode and the cavity, which is coupled to the waveguide, redirects the light coming from the emitter to the waveguide [6].

However, the design of PC cavities is not an easy task; it requires a considerable effort for the parameter search and optimization. Furthermore, since the simulation of high-Q cavities requires a long time, an empirical approach would not be practical [11]. In 2011, a deterministic design approach for ultra-high Q PC nanobeam cavities was developed [11], and it is this design and the previous work by Selim Scharmers [12] that the present work followed and continued for the fabrication of the cavities presented here.

# Chapter 1 Theory

Photonic crystals (PC) are periodic dielectric structures, this periodicity of the dielectric constant gives rise to a very interesting property “photonic band gaps”. This band gaps prevent light from certain range of frequencies to propagate inside the crystal and are the ones that will allows us to construct the nanobeam cavities presented in this work. Therefore, it is first necessary to understand the physics behind light propagation in photonic crystals and in this chapter a basic photonic crystals theory from Maxwell's equations will be presented along with some of the main properties of one-dimensional (1-D) photonic crystals. The theory that is presented in this chapter is based on the textbook by J .D. Joannopoulos et. al. [13] where the interested reader will find a more thorough derivation.

## 1.1 Maxwell's equations and the Eigenvalue problem

The behaviour of any electromagnetic wave traveling inside a dielectric media is governed by the Maxwell equations. In the present case the macroscopic Maxwell equations can be used since the dimensions of the dielectric structural features are larger than the atomic dimensions. In differential form and SI units, these equations take the form:

$$\nabla \cdot \vec{D}(\vec{r}, t) = \rho(\vec{r}, t), \quad \text{I}$$

$$\nabla \times \vec{H}(\vec{r}, t) - \frac{\partial \vec{D}(\vec{r}, t)}{\partial t} = \vec{J}(\vec{r}, t), \quad \text{II}$$

$$\nabla \times \vec{E}(\vec{r}, t) + \frac{\partial \vec{B}(\vec{r}, t)}{\partial t} = 0, \quad \text{III}$$

$$\nabla \cdot \vec{B}(\vec{r}, t) = 0. \quad \text{IV}$$

Where  $\vec{E}(\vec{r}, t)$  is the electric field,  $\vec{H}(\vec{r}, t)$  the magnetic field,  $\vec{D}(\vec{r}, t)$  the displacement field,  $\vec{B}(\vec{r}, t)$  the magnetic induction,  $\rho(\vec{r}, t)$  the free charge and  $\vec{J}(\vec{r}, t)$  the free current, all depending on the position vector  $\vec{r}$  and the time  $t$ .

Since only dielectric materials free of light sources are of interest, the following simplifications can be made:

- There are no free charges and currents within the medium of propagation

$$\rho(\vec{r}, t) = \vec{J}(\vec{r}, t) = 0$$

- In the case of  $\vec{B}(\vec{r}, t)$  and  $\vec{H}(\vec{r}, t)$ , the relative magnetic permeability for the majority of dielectric materials  $\mu_r(\vec{r})$  is almost one, so:

$$\vec{B}(\vec{r}, t) = \mu_0 \vec{H}(\vec{r}, t)$$

where  $\mu_0$  is the magnetic permeability in the vacuum.

And if the following two assumptions are taken:

- $\vec{E}(\vec{r}, t)$  and  $\vec{D}(\vec{r}, t)$  are linearly dependent

$$\vec{D}(\vec{r}, t) = \varepsilon(\vec{r}) \vec{E}(\vec{r}, t) \text{ where } \varepsilon(\vec{r}) = \varepsilon_0 \varepsilon_r(\vec{r})$$

- The dielectric constant  $\varepsilon(\vec{r})$  frequency dependence is ignored, by considering a small frequency range. Hence, a single value of the dielectric constant can be chosen.

Thus, the Maxwell equations I-IV take the form:

$$\nabla \cdot [\varepsilon_r(\vec{r}) \vec{E}(\vec{r}, t)] = 0, \quad \text{V}$$

$$\nabla \times \vec{H}(\vec{r}, t) - \varepsilon_0 \varepsilon_r(\vec{r}) \frac{\partial \vec{E}(\vec{r}, t)}{\partial t} = 0, \quad \text{VI}$$

$$\nabla \times \vec{E}(\vec{r}, t) + \mu_0 \frac{\partial \vec{H}(\vec{r}, t)}{\partial t} = 0, \quad \text{VII}$$

$$\nabla \cdot \vec{H}(\vec{r}, t) = 0. \quad \text{VIII}$$

To find solutions for these equations the separation of variable method can be employed, thus the solution is separated in the spatial and temporal variables (this will later lead to an eigenvalue equation for the spatial modes). Since, we restrict ourselves to solutions with constant frequency across time, the temporal part takes the form  $e^{-i\omega t}$ . Hence, these solutions are sinusoidal waves and can be written as:

$$\vec{H}(\vec{r}, t) = \vec{H}(\vec{r})e^{-i\omega t}, \quad \text{IX}$$

$$\vec{E}(\vec{r}, t) = \vec{E}(\vec{r})e^{-i\omega t}. \quad \text{X}$$

Inserting equations IX and X on V and VII give

$$\nabla \cdot \vec{H}(\vec{r}) = 0, \quad \text{XI}$$

$$\nabla \cdot [\varepsilon_r(\vec{r})\vec{E}(\vec{r})] = 0. \quad \text{XII}$$

which are the transversality requirements of the fields, this means that the fields are necessarily orthogonal to the direction of propagation of the electromagnetic wave.

Then substituting equations IX and X into VI-VII give

$$\nabla \times \vec{E}(\vec{r}) - i\mu_0\omega\vec{H}(\vec{r}) = 0, \quad \text{XIII}$$

$$\nabla \times \vec{H}(\vec{r}) + i\omega\varepsilon_0\varepsilon_r(\vec{r})\vec{E}(\vec{r}) = 0. \quad \text{XIV}$$

then, on dividing the bottom equation by  $\varepsilon_r(\vec{r})$  followed by taking the curl, it is possible to use equation XIII to eliminate  $\vec{E}(\vec{r})$  from XIV. Thus, obtaining a single equation in terms of  $\vec{H}(\vec{r})$ :

$$\nabla \times \left( \frac{1}{\varepsilon_r(\vec{r})} \nabla \times \vec{H}(\vec{r}) \right) = \left( \frac{\omega}{c} \right)^2 \vec{H}(\vec{r}) \quad \text{in which } c = \frac{1}{(\varepsilon_0\mu_0)^{-1/2}}. \quad \text{XV}$$

where  $c$  is the speed of light and  $\omega$  is the angular frequency of the wave. This last equation is known as the master equation because it contains all the information to be known about the modes  $\vec{H}(\vec{r})$ .

Furthermore, by defining the operator  $\hat{\theta}$  as:

$$\hat{\theta} = \nabla \times \left( \frac{1}{\varepsilon_r(\vec{r})} \nabla \times \right)$$

allows to rewrite equation XV:

$$\hat{\theta}\vec{H}(\vec{r}) = \left(\frac{\omega}{c}\right)^2 \vec{H}(\vec{r}). \quad \text{XVI}$$

This last equation XVI is an eigenproblem where the eigenvectors  $\vec{H}(\vec{r})$  are the field patterns of the modes and the terms  $\left(\frac{\omega}{c}\right)^2$  are the corresponding eigenvalues (from these eigenvalues the frequencies of the modes are extracted). Thus, the light propagation inside the dielectric structure is described by the solutions of equation XVI and the transversality condition of the field.

Furthermore, the operator  $\hat{\theta}$  turns out to be linear and Hermitian, and has the following consequences on the eigenvalues and modes:

- The eigenvalues  $\left(\frac{\omega}{c}\right)^2$  are real and positive. Therefore, the frequency of the modes is also real and positive.
- The modes  $\vec{H}_i(\vec{r})$  are mutually orthogonal.

### 1.1.1 Scaling property

There is a property due to the effect of the spatial scale. This property is present in equation XVI and it is important to point it out. This property shows that if a new system is formed by expanding (or compressing) a dielectric configuration, this new system will still behave the same way as the original system, but the modes for this new system will be expanded (or compressed) and the frequency will be reduced (or increased) accordingly.

To see this, let's modify the dielectric configuration  $\varepsilon_r(\vec{r})$  and let it be compressed or expanded by a factor  $s$ , so now there is a new dielectric configuration  $\varepsilon'_r(\vec{r})$ . This can be written as follows:

$$\varepsilon'_r(\vec{r}) = \varepsilon_r(\vec{r}/s). \quad \text{XVII}$$

letting  $\vec{r}' = \mathbf{s}\vec{r}$  results in  $x' = \mathbf{s}x, y' = \mathbf{s}y, z' = \mathbf{s}z$  (for each component of the vector), from it follows that  $\frac{\partial}{\partial x'} = \frac{1}{\mathbf{s}} \frac{\partial}{\partial x}$  (same for  $y$  and  $z$ ) and thus  $\nabla' = \nabla/\mathbf{s}$ . Then making the substitutions of  $\vec{r}$  and  $\nabla$  in XV gives:

$$\mathbf{s}\nabla' \times \left( \frac{1}{\varepsilon_r(\vec{r}'/\mathbf{s})} \mathbf{s}\nabla \times \vec{H}(\vec{r}'/\mathbf{s}) \right) = \left( \frac{\omega}{c} \right)^2 \vec{H}(\vec{r}'/\mathbf{s}). \quad \text{XVIII}$$

then, on dividing the previous equation by  $\mathbf{s}$  twice, one obtains:

$$\nabla' \times \left( \frac{1}{\varepsilon_r(\vec{r}'/\mathbf{s})} \nabla \times \vec{H}(\vec{r}'/\mathbf{s}) \right) = \left( \frac{\omega}{c\mathbf{s}} \right)^2 \vec{H}(\vec{r}'/\mathbf{s}). \quad \text{XIX}$$

finally, a new scaled version of the frequency  $\omega' = \omega/\mathbf{s}$  and the solution  $\vec{H}'(\vec{r}') = \vec{H}(\vec{r}'/\mathbf{s})$  can be defined, and since  $\varepsilon'_r(\vec{r}') = \varepsilon_r(\vec{r}'/\mathbf{s})$  one arrives at:

$$\nabla' \times \left( \frac{1}{\varepsilon'_r(\vec{r}')} \nabla' \times \vec{H}'(\vec{r}') \right) = \left( \frac{\omega'}{c} \right)^2 \vec{H}'(\vec{r}'). \quad \text{XX}$$

This last equation is the master equation for the new system, and it shows that the new system is just a scaled version of the original: The mode profiles are not changed (but they are scaled), and the frequencies of the modes are increased or decreased by the factor  $\mathbf{s}$ .

### 1.1.2 An important characteristic of the modes

To close this section, let us take a quick look at some properties of the modes  $\vec{H}$ , which will later help us understand the origin of the photonic bandgap.

The variational electromagnetic theorem [13]:

$$U_f(\vec{H}) = \frac{(\vec{H}(\vec{r}), \hat{\theta}\vec{H}(\vec{r}))}{(\vec{H}(\vec{r}), \vec{H}(\vec{r}))}. \quad \text{XXI}$$

where the inner product is defined as:

$$(\vec{H}, \vec{F}) \triangleq \int \vec{H}^*(r) \cdot \vec{F}^*(r) d^3r. \quad \text{XXII}$$

shows that the eigenfunctions  $\vec{H}$  of the system minimize the energy  $U_f$ . The lowest-frequency mode  $\vec{H}_0$  has the smallest eigenvalue  $\omega_0^2/c^2$  and this eigenvalue corresponds to minimum value of  $U_f$ . The next lowest eigenmode  $\vec{H}_1$  has the eigenvalue  $\omega_1^2/c^2$ , and it minimizes  $U_f$  while also satisfying the orthogonality constraint of the modes.

The physical consequence to be seen from equation XXI is better understood by rewriting XXI in terms of the electric field:

$$U_f(\vec{H}) = \frac{(\nabla \times \vec{E}, \nabla \times \vec{E})}{(\vec{E}, \epsilon_r \vec{E})} = \frac{\int |\nabla \times \vec{E}(\vec{r})|^2 d^3r}{\int \epsilon_r(\vec{r}) |\vec{E}(\vec{r})|^2 d^3r}. \quad \text{XXIII}$$

Now, the denominator in XXIII tells us that concentrating the electric field in regions of high dielectric reduces the energy of the mode. Thus, the lowest frequency mode  $\vec{H}_0$  will lower its energy by concentrating mostly in the high dielectric material. The higher order modes, due to the orthogonality condition of the modes, will be pushed out of the high dielectric material, hence they cannot concentrate their electrical field in the high dielectric material. The numerator will be small or big depending on the electric field spatial distribution.

## 1.2 Photonic crystals

As mentioned before the photonic crystals are categorized as one-dimensional (1-D), two-dimensional (2-D) and three-dimensional (3-D) crystals according to the dimensionality of their building blocks, see Fig. 1. 1-D PC are formed by placing alternate layers of two different materials which have low and high dielectric constants, therefore the dielectric constant is modulated along one direction. In 2-D photonic crystals, the dielectric constant is periodic along two directions and extends to infinity in the third direction. In the 3-D structures, the dielectric constant is periodic along the three directions. This work is only concern with 1-D photonic crystals,

which are the simplest possible PCs, and in this section the most important features of the PCs will be discussed.

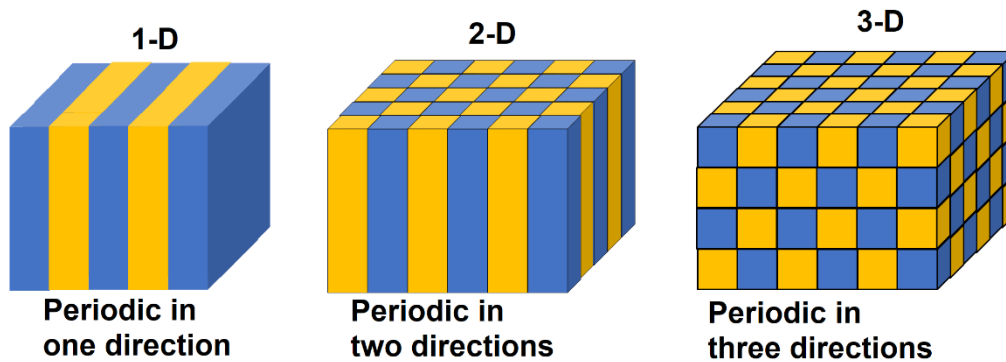


Fig. 1 Photonic crystals with dielectric periodicity in one, two, and three dimensions. This figure was adapted from [13].

The 1-D photonic crystals are systems that has discrete translational symmetry in one direction. Consequently, if a displacement is performed in the direction of the discrete symmetry by a multiple of the periodicity length  $a$  (known as lattice constant), then the value of  $\epsilon_r$  does not change when the displacement  $\vec{a}$  is performed, and this can be written as:

$$\epsilon_r(\vec{r}) = \epsilon_r(\vec{r} \pm \vec{a}) \quad \text{XXIV}$$

where  $\vec{a}$  is known as the primitive lattice vector. Since the structure of interested is assumed to be periodic in one direction ( $x - axis$ ), the lattice vector will be defined as  $\vec{a} = a\hat{x}$  (Fig. 2). The repeating dielectric structure defined by the width  $a$  in Fig. 2 is known as unit cell, and it is the smallest repeating unit of the structure.

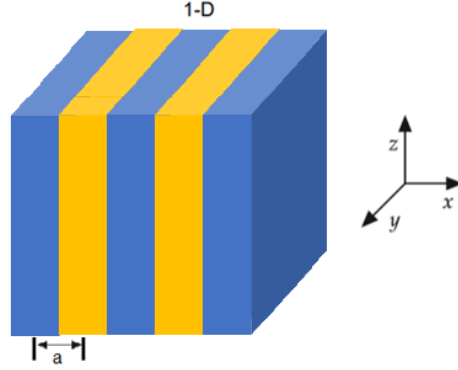


Fig. 2 Dielectric configuration in one dimension. The lattice constant is indicated. This figure was adapted from [13].

Now, the solutions for the multilayers structure shown in Fig. 2, in which the structure possess discrete translational symmetry in  $x$ , are already known. The solutions  $\vec{H}(\vec{r})$  are given by Bloch's theorem, and for periodicity in one dimension ( $x$ -axis for the present case), the solutions have the form [13]:

$$\begin{aligned} \vec{H}_k(\vec{x}) &= \sum_m \vec{C}_{k_x, m}(y, z) e^{i(k_x + m \frac{2\pi}{a})x}, \\ &= e^{i(k_x \cdot x)} \sum_m \vec{C}_{k_x, m}(y, z) e^{i(mb)x}. \end{aligned} \tag{XXV}$$

where the term  $\vec{b} = \frac{2\pi}{a} \hat{x}$  is known as the reciprocal lattice vector. The summation term is just a Fourier series, hence it can be any function. Thus, equation XXV can be rewritten as

$$\vec{H}_k(\vec{x}) = e^{ik_x \cdot x} \vec{u}_{k_x}(x, y, z). \tag{XXVI}$$

where  $\vec{u}_{k_x}$  represents any function with period equivalent to lattice constant  $a$ . This means that  $\vec{u}_{k_x}(x, y, z) = \vec{u}_{k_x}(x + ma, y, z)$ .

The solutions  $\vec{H}(\vec{r})$  in equation XXVI are known as Bloch states and they consist of plane waves modulated by a periodic function  $\vec{u}_{k_x}$ . Furthermore, the Bloch states with wave vector that differed by a multiple of the reciprocal vector  $\frac{2\pi}{a}$  have the same eigenvalues. Hence, if the reciprocal vector value is divided by two and this result is set as upper positive and lower negative boundary, a region, without the

degeneracy previously mentioned, is defined. This region is known as the Brillouin zone, and is given by:

$$\frac{-\pi}{a} < k_x < \frac{\pi}{a} \quad \text{XXVII}$$

and since no degeneracy is present in this region, it is enough to examine the solutions in this space of wave vectors.

Now, let us extend the previous result to three dimensions. For this let us remember again what a three dimensional photonic crystal is: it is a system with discrete translational symmetry in three directions. Hence, to extend Equation XXVI to 3 dimensions it is first necessary to take the following changes: the lattice vector is defined in terms of three primitive lattice vectors  $a_1, a_2, a_3$ , to account for the discrete translational symmetry in three directions,  $\vec{R} = la_1 + ma_2 + na_3$  ( $l, m$  and  $n$  are integers). Now, the periodic function  $u_k(\vec{r})$  satisfies the condition  $u_k(\vec{r}) = u_k(\vec{r} + \vec{R})$  and the dielectric constant satisfies  $\epsilon_r(\vec{r}) = \epsilon_r(\vec{r} \pm \vec{R})$ . The three dimensional reciprocal lattice vector is  $\vec{k} = k_1b_1 + k_2b_2 + k_3b_3$  and it consist of three primitive reciprocal lattice vectors  $b_1, b_2, b_3$ . These primitive reciprocal lattice vectors satisfy the relation  $\vec{a}_i \cdot \vec{b}_j = 2\pi\delta_{ij}$ . Finally, the Bloch state can be written as

$$\vec{H}_k(\vec{r}) = e^{i\vec{k}\cdot\vec{r}} u_k(\vec{r}). \quad \text{XXVIII}$$

With the form of the solutions known, let us substitute the Bloch state into the Master Equation (XV). This will provide a better understanding of the band structure for photonic crystals:

$$\hat{\theta} \vec{H}_k = \left(\frac{\omega(\vec{k})}{c}\right)^2 \vec{H}_k, \quad \text{XXIX}$$

$$\nabla \times \frac{1}{\epsilon_r(\vec{r})} \nabla \times e^{i\vec{k}\cdot\vec{r}} u_k(\vec{r}) = \left(\frac{\omega(\vec{k})}{c}\right)^2 e^{i\vec{k}\cdot\vec{r}} u_k(\vec{r}).$$

Using twice the identity  $\nabla \times \gamma \vec{B} = \gamma(\nabla \times \vec{B}) + (\nabla \gamma) \times \vec{B}$  and dividing by the exponential term:

$$(\nabla + i\vec{k}) \times \frac{1}{\varepsilon_r(\vec{r})} (\nabla + i\vec{k}) \times u_k(\vec{r}) = \left(\frac{\omega(\vec{k})}{c}\right)^2 u_k(\vec{r}). \quad \text{XXX}$$

identifying the left-hand side term as the new Hermitian operator  $\hat{\theta}_k$

$$\hat{\theta}_k \triangleq (\nabla + i\vec{k}) \times \frac{1}{\varepsilon_r(\vec{r})} (\nabla + i\vec{k}) \times. \quad \text{XXXI}$$

it yields

$$\hat{\theta}_k u_k(\vec{r}) = \left(\frac{\omega(\vec{k})}{c}\right)^2 u_k(\vec{r}). \quad \text{XXXII}$$

With a quick look at  $\hat{\theta}_k$  is possible to notice that the new operator  $\hat{\theta}_k$  depends now on the wave vector  $\vec{k}$  and acts on the periodic function  $u_k(\vec{r})$  instead of  $\vec{H}_k$ . Furthermore, the solutions for the light propagating inside the photonic crystal are now given by equation XXXII along with the conditions of transversality and periodicity:

$$(\nabla + i\vec{k}) \cdot u_k = 0, \quad u_k(\vec{r}) = u_k(\vec{r} + \vec{R}). \quad \text{XXXIII}$$

and analogous to the one dimensional case (thanks to the periodicity of the modes) it is possible to restrict the eigenvalue problem to the Brillouin zone (XXVII).

As mentioned before, the Bloch states were substituted in the master equation to get a better understanding of the band structure for photonic crystals, so let us keep in the mind the remarks previously made and address now the band structure. The band structure of the photonic crystal describes the range of allowed frequencies that the light might have when traveling inside the photonic crystal. If  $\vec{k}$  is fixed, one would obtain a set of discrete frequencies from the eigenvalues for each mode. But since  $\vec{k}$  is a continuous variable, if one moves to the next values of  $\vec{k}$  and obtains their respective set of discrete frequencies, at the end one would obtain an infinite set of discrete frequency bands (Fig. 3). These bands are classified with an integer number  $n$  which is known as band number. The plot of these bands as function of the wavevector is known as band structure.

To conclude, the band structure provides most of the information required for designing photonic crystal. Thus, to extract the band structure, a huge effort has been made to develop methods for computing the solutions of the eigenvalue problem of equation XXXII. One of these methods is FDTD (Finite-Difference Time-Domain) and it will be addressed on the next chapter.

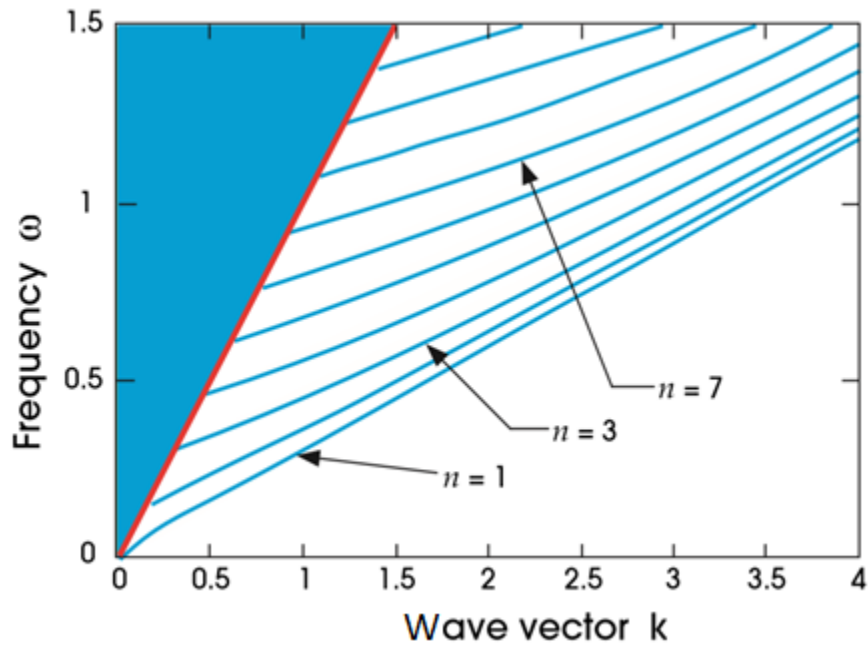


Fig. 3 Example of mode frequencies bands, the blue lines correspond to the modes localized in the dielectric. This figure was taken from [13].

### 1.2.1 The origin of the photonic band gap

A complete photonic band gap is a range of frequencies in the band structure where there are not allowed modes for the light to propagate [13]. Hence, it does not matter which magnitude of  $\vec{k}$  the mode possesses, and it does not matter the direction of propagation of the light, if the frequency of the mode is inside the range of forbidden frequencies by the band gap then it cannot propagate inside the photonic crystal, see Fig. 4.b).

To understand the origin of the photonic band gap, let us once again consider the multilayer system with periodicity  $a$  of Fig. 2. Let us not forget that the multilayer system is a one-dimensional photonic crystal, and it consist of two intercalated

materials with different dielectric constants. The band structure, also known as dispersion relation, for this multilayer system is shown in Fig. 4 (b).

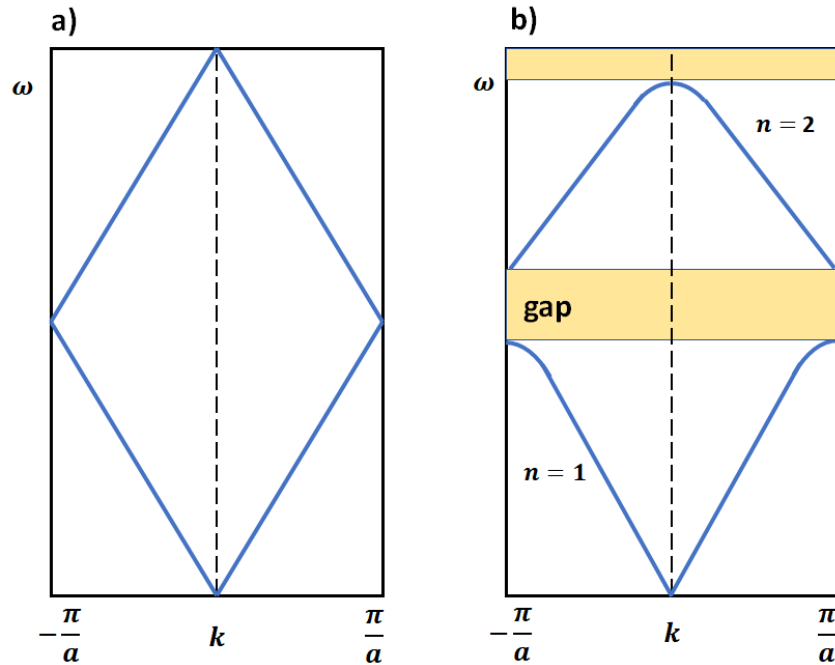


Fig. 4 Dispersion relation (band structure), frequency  $\omega$  vs wavenumber  $k$  of a: a) uniform medium. b) Effect on the bands of a physical periodic dielectric variation  $\Delta\epsilon_r > 0$ . This figure was adapted from [13].

Now, let us consider the case when the materials of the multilayer system have the same dielectric constant  $\epsilon_r$  so that  $\Delta\epsilon_r = 0$ . In this case light sees no distinction between the materials and it behaves as if it was propagating inside a homogenous medium. For a homogenous medium the dispersion relation has the form [13]:

$$\omega(k) = \frac{ck}{\sqrt{\epsilon_r}}, \quad \text{where } c \text{ is the speed of light}$$

this is depicted in Fig. 4 (a), just that a periodicity  $a$  has been imposed and as a result the band bends back inside when reaching  $-\frac{\pi}{a}$  and  $\frac{\pi}{a}$ . Now, let us take a closer look to both plots a) and b) from Fig. 4. Both plots look alike, but there is an important difference, plot a) has no band gap and a value of  $\Delta\epsilon_r = 0$  while plot b) has a band gap and a value of  $\Delta\epsilon_r > 0$ . Thus, the band gap only appears if  $\Delta\epsilon_r > 0$ .

From the previous observations, it is easy to mistakenly think that the origin of the band gap is due to the dielectric contrast difference, but by taking a look again at the

variational principle (equation XXIII) and the remarks of that section **1.1.2**, it is possible to get a better understanding of the physical origin of the photonic bandgap.

In section **1.1.2**, it was found that the way to minimize the function from equation XXIII, is by concentrating the electric field in regions of high dielectric constant  $\epsilon_r$ . This means that the modes under the gap, see Fig. 4.b), which correspond to the first eigenvalue of every solution for each  $k$ , tend to concentrate most of their energy in high dielectric regions. While the modes above the gap, which correspond to the second eigenvalue, concentrate less energy in the high dielectric region because they are pushed out by the orthogonality condition. Thus, the gap arises from this difference in field location.

Finally, let us remember that we were dealing with a 1-D photonic crystal, this means that the photonic band will only exist in the direction of periodicity. Consequently, 1-D photonic crystal do not form a complete band gaps, instead they form something called incomplete band gaps, which only exist over wavevectors in one certain direction. Thus, to create a complete band gap a 3-D photonic crystal would be need it. In either case, 1-D, 2-D or 3-D photonic crystals, the origin of the complete or incomplete gaps are the same [13].

### **1.2.2 Defects and cavities**

To conclude this chapter, this last section will address another important aspect of photonic crystals: defects. The introduction of a defect in the crystal structure of a 1-D photonic crystal, can be done for example: by increasing the width of one of the layers or by changing the value of  $\epsilon_r$  in just one of the layers. Either way this breaks the periodicity of the lattice and gives rise to the existence of a localized mode. The key feature here, is when the defect is done in a way so that the localized mode is introduced into the photonic band gap, thus creating a cavity, see (Fig. 5). This is analogous to the creation of energy levels inside the semiconductor band gap, in this case this is achieved by doping the semiconductor, which is the intentional introduction of impurities into the semiconductor.

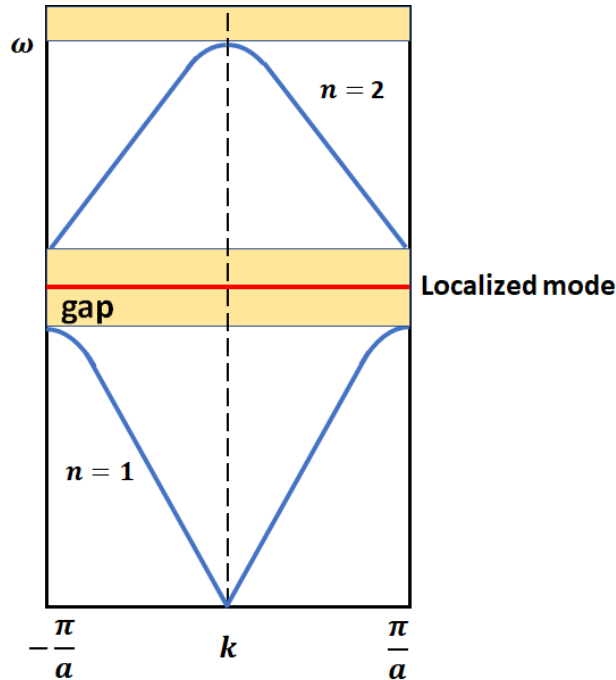


Fig. 5 Band structure with a defect inside the photonic bandgap. This figure was adapted from [13].

For 1-D photonic crystals, the cavity is formed by employing two Bragg mirrors inside a waveguide, one at each end of the cavity. These mirrors usually are formed by making an array of air-holes in the dielectric, thus creating the multilayer system with periodicity  $a$ , see (Fig. 6). For this array, the defect can also be introduced by modifying one or more air-holes, hence, breaking the periodicity of the lattice.

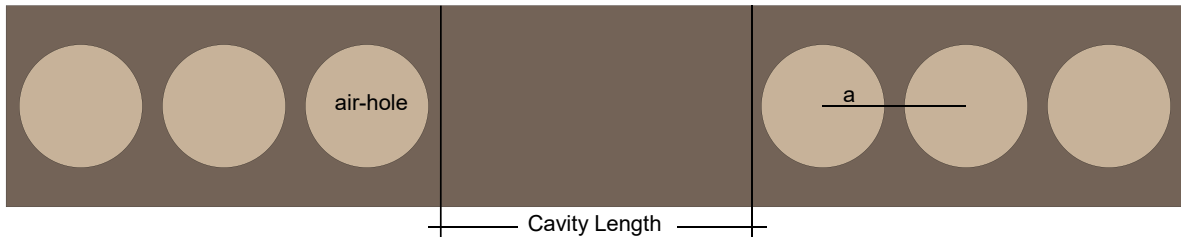


Fig. 6 1-D Photonic Crystal cavity with Bragg mirror in both sides and periodicity  $a$ .

Finally, let us summarize what the Quality factor is. The Quality Factor  $Q$  is a dimensionless quantity used to measure the losses of a cavity. This  $Q$  factor is defined as the ratio of stored energy and the loss of energy per cycle [13]:

$$Q = \omega_0 \frac{\text{Energy stored}}{\text{Power loss}} \quad \text{XXXIV}$$

where  $\omega_0$  is the resonant frequency of the cavity.

From equation XXXIV it can be seen that if a cavity has a high  $Q$  then the cavity has small losses and consequently it can store energy for a longer period of time. If there were zero losses, then the cavity in principle could store energy during an indefinite time. Unfortunately, losses are always present in any fabricated cavity, and they will limit the achievable values of the quality factor. In the case of 1-D photonic crystal reducing the losses becomes quite challenging since the photonic crystal only traps light in one direction. Thus, to confine light in the other two directions the cavity relies in total internal reflection.

## Chapter 2 Modelling of photonic structures

When designing photonic structures, there are two approaches for evaluating and optimizing the parameters of the structures one desires to fabricate: the first one is to just directly fabricate the structures while making variations of the parameters for each sample, so the parameters are optimized by trial and error. The second option is to first simulate the structures, using a commercial software like Lumerical [14].

The first option might be fast for very simple structures, but it can also be costly to fabricate them and time consuming to perform the experimental measurements. On the other hand, simulating the desired structures can provide a better understanding of the structures because for some complex geometries the solutions might not be intuitive or there might not be any known analytical solution. In addition, simulations can be used to verify experimentally obtained results, while having the advantages of time efficiency and lower cost. Generally, a mixture of both approaches leads to the most time efficient method when fabricating the nanostructures.

In the past years, the simulation of photonics structures has matured so much that nowadays it might not be necessary to be concerned about the finer details of the numeric methods used to solve the Maxwell equations. However, it is still important to have basic understanding of the theory behind the simulation software for photonics, so in the next section a summary of the most important aspects of the utilized software Lumerical FDTD will be presented.

### 2.1 Lumerical FDTD

The FDTD-Method (Finite-Difference Time-Domain) numerically solves Maxwell equations in differential form by providing a way to obtain the future fields from the past fields (thus a starting electromagnetic field is needed). This allows to tackle a wide range of complicated problems, but the key feature of this method is that in a single simulation run it can obtain the response of the system for a wide range of frequencies. The drawback of this method is that most of the times it is

computationally expensive, therefore the solutions might require a considerably amount of computer memory and computation time. The method is efficient when the dimensions of the physical features for the structures of interest are on the order of the wavelength size. Hence, is important to keep this mind, if for example the wavelength is very small compared to the physical features of the structures of interest, although FDTD would be able to provide accurate results, a ray-based method might provide a more efficient way to address the problem and with a similar accuracy [15].

The FDTD algorithm can be summarized as follows (a more detailed explanation of the method can be found at [15] and [14]). First the space and time is discretized, consequently it is divided into small segments. With time and space discretized it is possible to apply the numerical method known as finite difference for solving differential equations, therefore one works with the differential form of the Maxwell equations. Then by applying the finite difference method, one obtains one pair of equations which give the electric and magnetic fields one step in the future in terms of the past fields. Second, the magnetic field is computed one step into the future. Then after computing the magnetic field first, the electric field is computed one step into the future. Finally, with the new updated fields it is possible to compute the fields one more step into the future where the previously computed field are the past fields for this new computation. This process is repeated until reaching the desired time in the future. It is important to keep in mind that due to the discretization of time and space for solving the differential equations, it is not possible to compute the electric and magnetic fields at the same point in space or at the same point in time, therefore to overcome this problem FDTD software like Lumerical use the interpolation method to compute this missing points of data.

Lumerical FDTD, as the name indicates, is a commercial software which employs the Finite-Difference Time-Domain method to solve the Maxwell equations. The software can be used to design, analyze, and optimize photonic devices. As mentioned before the FDTD-method requires and starting electromagnetic field, hence, the software counts with several types of common sources when exciting

photonic devices such as: dipoles, beams, plane waves, a total-field scattered-field (TFSF) source, a guided-mode source, and custom sources.

### 2.1.1 Mesh size

One key aspect when running a simulation with this software is the mesh size of the simulation region. Lumerical uses a rectangular mesh, like the one shows in Fig. 7, and it is at each mesh point where the simulation quantities (material properties, geometrical information, electric and magnetic field) are calculated. Therefore, using a smaller mesh would give more accurate results, for example: as it can be seen in figure 7 (a) and (b) the depicted circle perimeter becomes more uniform as the mesh size becomes smaller.

However, using a finer mesh comes with a cost, the simulation time and memory requirements will increase as the mesh becomes smaller. Thus, the simulation time and memory requirements will increase as a function of the mesh step ( $dx$ ). In the case of 3D simulations, the memory requirements and simulation time grow as follows:

$$\text{Memory requirements} \approx \left(\frac{1}{dx}\right)^3 \quad \text{Simulation time} \approx \left(\frac{1}{dx}\right)^4$$

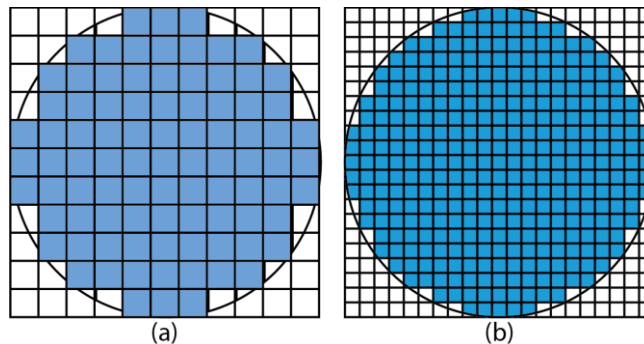
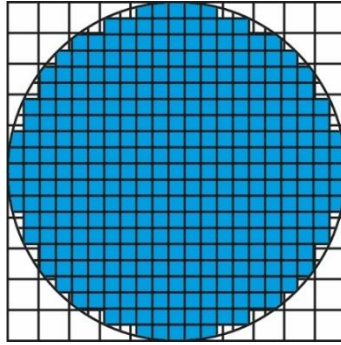


Fig. 7 a) Applying a big mesh step size to depict the circle, b) Applying a finer mesh to depict the circle.

To try to mitigate this it is possible to implement in Lumerical mesh override regions, which allows the user to define structures or regions of space with a finer mesh, thus the simulation time will be smaller than the case with uniform small mesh size. This can be seen in Fig. 8, where the circle has a mesh override region, the circle has the

same mesh size as Fig. 7 (b) but its surroundings has the same mesh size as Fig. 7 (a). If a light source was placed and the simulation was to be to run the simulation time would be considerable less in the case of Fig. 8, than the simulation time of the Fig. 7 (b) which has uniform mesh over all region.



*Fig. 8 Circle with mesh override region, the circle has a finer mesh than its surroundings.*

### **2.1.2 Boundary conditions**

Another important aspect when implementing the simulation is the simulation boundaries. In the previous sections, what happens at the mesh endings or how to terminate the grid were not mentioned. For example, one might be interested on simulating the propagation of the fields in a small region from an open space or depending on the application it might be necessary to reflect the fields back into the simulation area. The solution to this are the boundary conditions, and many have been proposed in the literature. In the case of Lumerical it supports PML (Perfectly Matched Layer), metal, periodic, Bloch and PMC (Perfect Magnetic Conductor) boundaries. In this work only PML boundaries were used.

The PML (Perfectly Matched Layer) is the most commonly used absorbing boundary condition, that has extremely small reflection. These boundaries attempt to absorb all the outgoing fields from the simulation region, without reflecting them back to the area of interest. However due to the numerical nature of the FDTD-method, perfect absorption is not possible, thus a very small field is reflected and lingers throughout the grid. More detailed information of this boundary can be found in [16].

So far in this chapter a summary of the modelling technique for the photonic structures was presented, in a general approach the modelling theory was discussed, and the important simulation components needed to obtain accurate results while modelling photonic structures were reviewed. These parameters (light source, simulation region with boundary conditions and mesh size) are depicted on Fig. 9. But there is one more key thing to assess in this chapter, the calculation of the Q-factor of the simulated cavities.

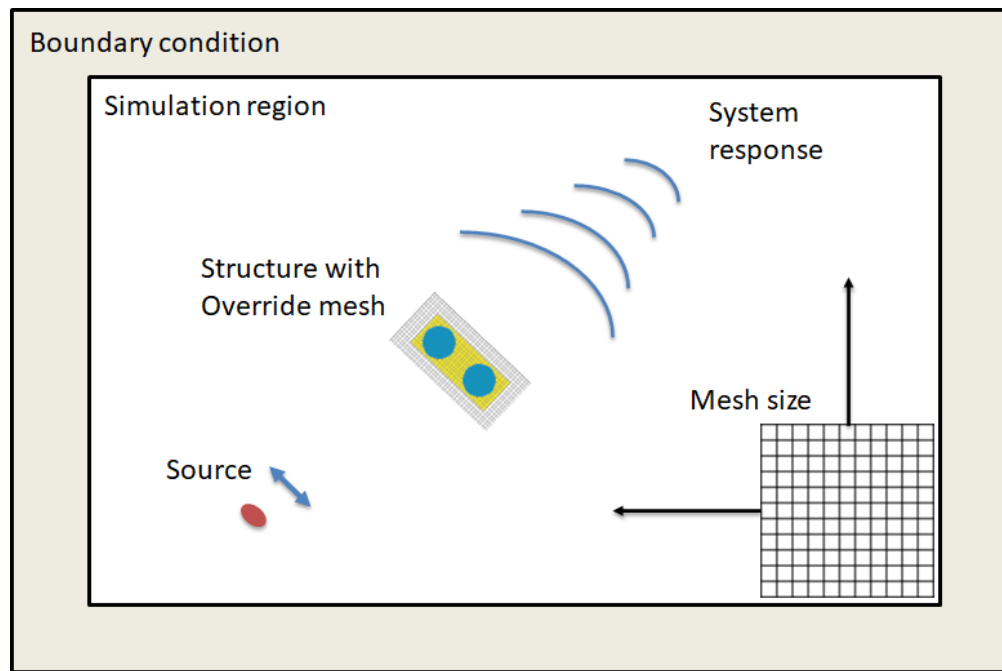


*Fig. 9 Schematic of the main simulation components.*

### 2.1.3 Q-factor calculation

There are two methods for extracting the Q factor when using Lumerical FDTD, choosing the suitable method leads to accurate results and avoids extra work and computation time for simulating the cavities. Lumerical FDTD divides cavities in two classes: low Q value cavities and high Q value cavities.

A low Q value cavity is a cavity which electromagnetic fields fully decays during the simulation in an amount of time that can be simulated by FDTD with a reasonable amount of computational resources and computational time. If the decay time is too

long, then more memory and simulation computational time would be need it, making at some point the simulation not feasible.

Thus, if the cavity has short decay time of the electromagnetic fields, then the best method for extracting the Q value is from the frequency spectrum. The Q is defined as the ratio of the resonant frequency  $\omega_r$  of the mode and the full width at half maximum FWHM of the resonance in the spectrum [13].

$$Q = \frac{\omega_r}{FWHM} \quad \text{XXXV}$$

If the cavity has a very long decay time of the mode therefore a high Q value, then in this case, is not possible to extract the Q value from the frequency spectrum because the FWHM of the resonance peak would vary with the simulated time. This last point can be easily understood by means of the Fourier transform of a rectangular pulse (Fig. 10), where the width of the main lobe in the frequency domain varies as  $\frac{1}{T}$  where  $T$  is the duration in time of the pulse, and by remembering that the rectangular pulse can be modulated by any function (in the current situation  $T$  would be the simulated time). In the case of a high Q value cavity, the Q value can be extracted from the slope of the envelope of the decaying mode, using the formula:

$$Q = \frac{-\omega_r \log_{10}(e)}{2m} \quad \text{XXXVI}$$

where  $m$  is the slope of the decay. The derivation of the above equation can be found in [14].

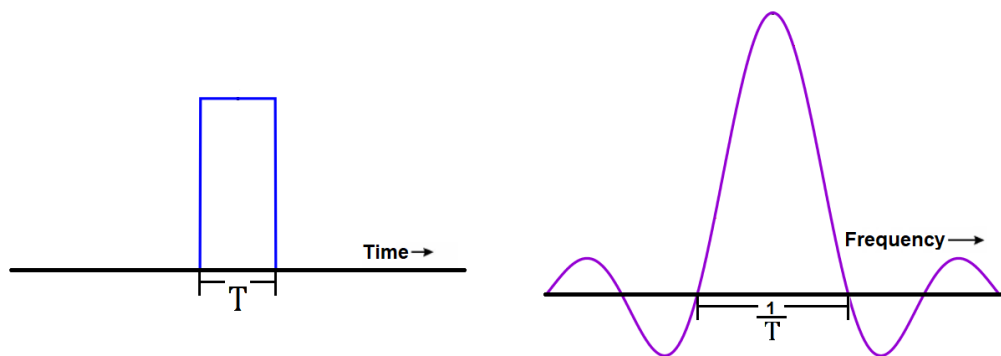


Fig. 10 Fourier transform of a rectangular pulse.

## Chapter 3 Fabrication

In this chapter, the processes involved in the fabrication of the nanobeam cavities are described. In order to fabricate the desired cavities the structure design from Fig. 6 was chosen, due to its simplicity, good coupling efficiency with a waveguide, and achievable high quality factors along with small mode volumes (comparable to those found in 2-D photonic crystal cavities) as demonstrated in previous works [17, 18, 19, 20]. In this work, the optimization of the parameters of the structure were done for a  $Si_3N_4$ -on- $SiO_2$  platform following the same deterministic method outline in [11]. The flow chart below Fig. 11 presents all the steps performed to fabricate the cavities. Since any small contamination (like dust particles, aerosol particles or particles coming from the body) could potentially interfere with the fabrication process or affect the purity of the materials been used, therefore ruining the quality of the manufactured devices or even leaving the manufactured devices completely useless, the fabrication procedures must be carried out inside clean room facilities. Clean rooms are controlled environments which can guarantee a working space with extremely low levels of contaminants.

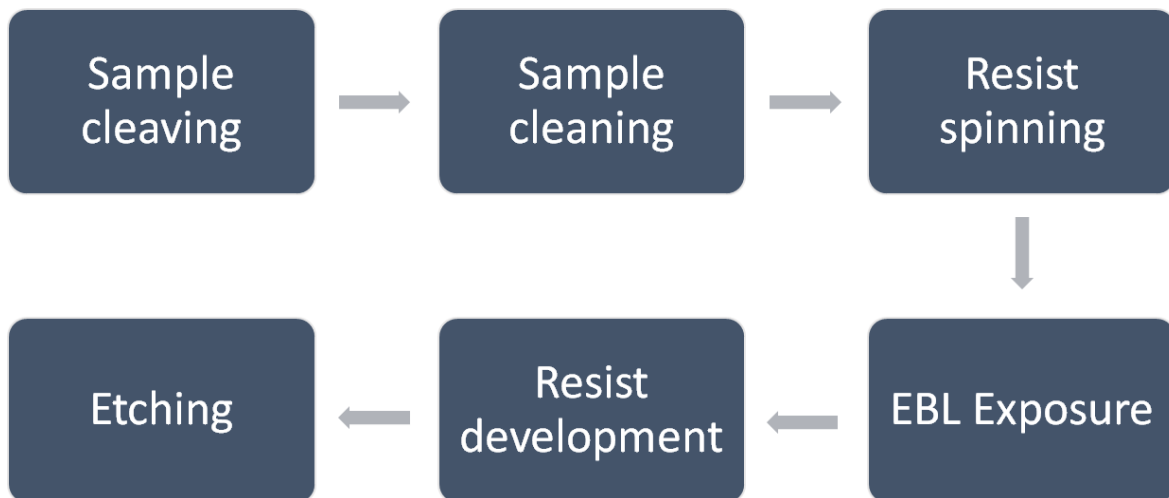


Fig. 11 Flow-chart showing steps of the fabrication process

### 3.1 $Si_3N_4$ -on- $SiO_2$ platform

One of the most notable platforms for the development of photonic integrated circuits is silicon, not only because silicon is the second most abundant element in earth, but it also offers two important properties: high refractive index contrast and complementary metal-oxide-semiconductor (CMOS) fabrication compatibility [21] [22]. CMOS fabrication refers to the semiconductor manufacturing processes, which nowadays are well mastered, for integrated circuits based on silicon.

Nowadays, most silicon products are built on silicon-on-insulator (SOI) platform with high index contrast (3.5 vs 1.5), but SOI only provides low absorption losses in the wavelength range from 1.1  $\mu\text{m}$  - 3.7  $\mu\text{m}$  [22]. On the other hand, the  $Si_3N_4$ -on- $SiO_2$  platform has moderate index contrast (2 vs 1.5), low absorption losses on the wavelength range from 400 nm - 2.35  $\mu\text{m}$  [21], and it is also compatible with the standard CMOS processing, thus allowing the fabrication of extremely compact photonic circuits.



Fig. 12 Schematic of  $Si_3N_4$ -on- $SiO_2$  platform.

### 3.2 Cleaving

Crystalline solids (crystals) consist of a structure of atoms or molecules arranged in a fixed and repeating three-dimensional pattern. This pattern has a definite geometrical shape. When some external pressure is applied to a crystalline solid, thus breaking it, it will have a tendency of splitting along a particular plane of its structure (where the bonding forces are the weakest), this plane is known as cleavage plane or crystallographic plane Fig. 13. The breaking up of a larger crystal,

along its cleavage plane, into smaller ones is known as cleaving. The resulting crystals will have smooth faces.

For this work a 11mm x 11mm chip and a 11mm x 7mm chip were cleaved from a  $Si_3N_4$ -on- $SiO_2$  wafer. The cleaving was performed by scratching the sample surface with a diamond tip, after it the sample can be easily broken using a couple of pliers.

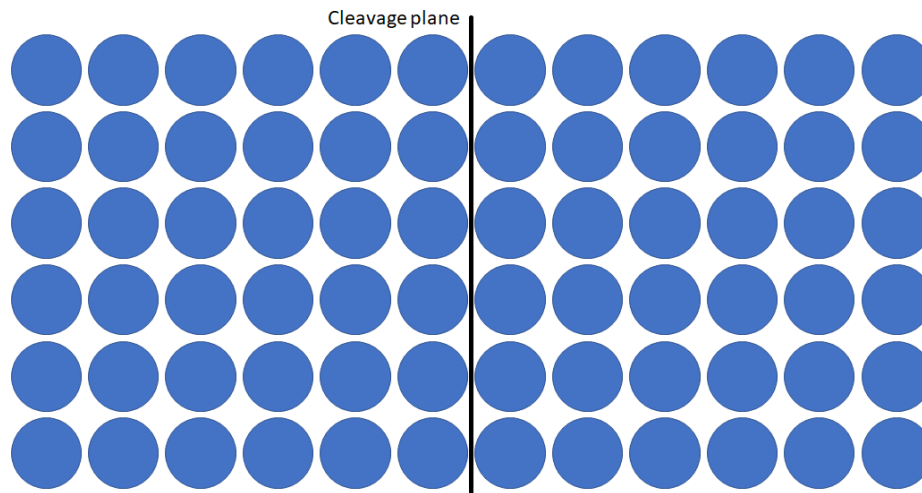


*Fig. 13 Diagram of a crystalline solid and location of its cleavage plane*

### 3.3 Cleaning and Spin-coating

To have a high adherence between the chip and the resist that will be applied later during the spin-coating procedure, it is first necessary to clean the chips surfaces from any organic materials that they might have stick to them. Thus, two ultrasonic baths with different organic solvents are performed: first a bath in acetone followed by another bath in isopropyl alcohol (IPA), for 5 minutes each. It is important to perform the baths in this order, otherwise the acetone could leave a small layer of residue on the chips surfaces which would reduce the adherence with the resist. The chip is not allowed to self-dry after each cleaning procedure: once the acetone bath is done the chip is rinse with IPA and later placed in IPA for the second bath, then when the second bath is completed the excess of IPA is removed with a nitrogen gun.

Spin-coating is a common method for applying a thin resist film on substrates. This spin-coating method can achieve a highly homogenous film of resist and allows control of the film thickness by adjusting the speed at which the sample is rotated. Some alternative methods are spray-coating and dip-coating. At the beginning of the spin-coating method a small quantity of the resist is dropped on the surface of the sample. Then, during the sample spinning, the centrifugal force is responsible for distributing the resist across the surface of the sample. Generally, the samples are spun at a speed starting from 1000 rpm to 8000 rpm [23]. If the sample was already spinning when the resist was applied the method is known as dynamic spin coating, and if the sample is spun after the application of the resist the method is known as static spin coating Fig. 14. Dynamic spin coating is used when either the resist or substrate has poor wetting abilities [24]. Finally, while the sample is spinning, part of the solvent of the resist is evaporated leading to stop of the thinning process (the rest of the solvent is evaporated by baking the sample afterwards).

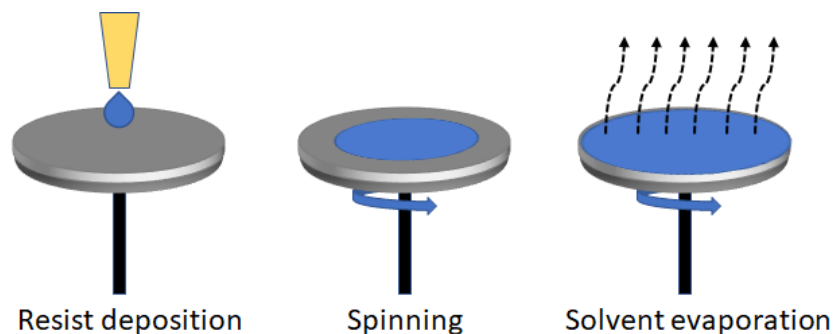


*Fig. 14 Schematic of static spin coating process.*

In this work the samples were static spin coated with a positive resist layer, CSAR-62 from Allresist company, of approximately 330 nm. This thickness is achieved at speed of 2000 rpm for 60 seconds. Next, for evaporating the remaining solvent in the resist and temper it, the samples are baked at 150°C during 60 seconds on a hot plate in accordance with the data sheet [25].

### 3.4 Lithography and Development

Once spin coating is completed, the next step is to print the desired pattern onto the chip's surface. Then, to be able to print the pattern on the chip a process known as lithography is employed. There are two lithography techniques commonly used for printing the pattern on the chip: photolithography and e-beam lithography.

In photolithography, a patterned mask is placed above the chip and then it is illuminated, the mask protects certain areas of the photo-sensitive resist from the incoming light, and allows light to reach to other areas of the resist. Consequently, the pattern is printed on the resist. In the case of electron beam lithography, also known as e-beam lithography or EBL, the electron beam is directly focused on the surface of the sample and thus allowing the electron-sensitive resist to be scanned. During the scanning, the designed pattern is drawn on the chip's surface, hence the use of a mask is not needed. Since EBL does not require a mask, EBL is highly flexible when the pattern design needs to be modified and makes this method suitable for prototyping. The pattern for EBL can be designed using software like AutoCAD, Klayout<sup>1</sup>, Beamer<sup>2</sup> and Raith toolbox for Matlab<sup>3</sup>, for giving some examples.

In the case of EBL the resolution depends on the electrons interaction with the resist. On the other hand, photolithography is limited by diffraction. The smallest reported feature sizes found for photolithography are at 40nm [26]. While in the case of e-beam lithography there are reports of feature sizes below 10 nm [27], but in most cases, by really working at it, 10 nm is the limit.

After exposing the resist to the e-beam the next step is development, which is the process of dissolving the resist. Due to the e-beam exposure the solubility of the exposed areas changes, thus allowing us to dissolve the resist with an agent (usually called developer). There are two kinds of resist that can be used: positive or

---

<sup>1</sup> KLayout – Mask Layout: <https://www.klayout.de>

<sup>2</sup> GenISys Advancing the Standard – Beamer: <https://www.genisys-gmbh.com/beamer.html>

<sup>3</sup> See reference [21].

negative, see Fig. 15, depending on which one is been used the exposed area of the resist is dissolved by the developer (positive resist) or remains (negative resist). On a negative resist, only the unexposed areas are dissolved by the developer.

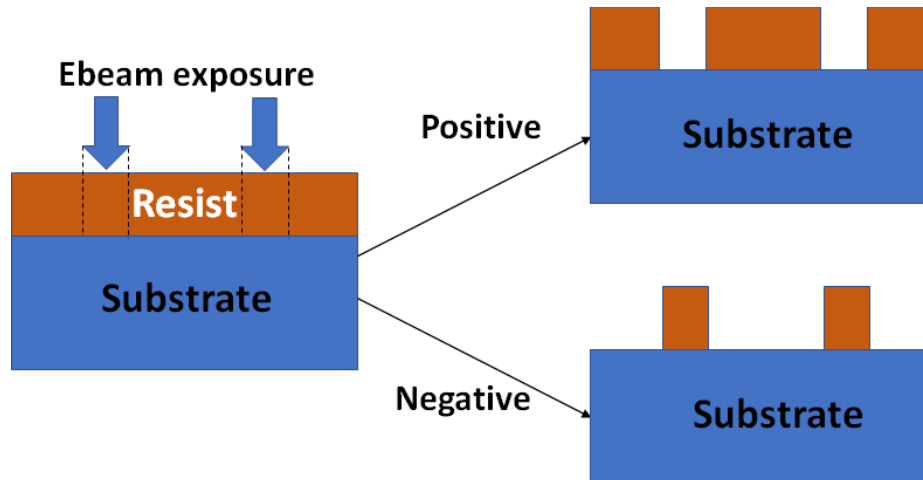


*Fig. 15 Schematic of positive and negative resist after chemical developing*

In this work the patterns were defined by electron beam lithography on a Voyager unit from the company Raith Nanofabrication with a dose of  $160 \frac{\mu\text{C}}{\text{cm}^2}$ . Followed by development dipping the chip in AR 600-546 from Allresist for 70 seconds and moving the chip slowly all the time. Then the chip is rinse with IPA for 30 seconds to remove any remainings of the AR 600-546. Finally, after removing the IPA with the air gun, the chip is bake again on a hot plate for 1 minute at  $130^\circ\text{C}$ . All the patterns for the EBL were created with the Raith toolbox for Matlab [28] and from previous designs made by Selim Scharmiers [12].

### 3.5 Etching

Now, in order to fabricate the desired nanostructures, the pattern of the resist needs to be transferred onto the underlying material. To achieve this, it is necessary to remove the material that is no longer protected by the resist and this process is known as etching.

The unprotected material can be removed via two methods: dry etching or wet etching. Dry etching techniques use plasma to etch the sample by bombarding it with

ions which physically eject the atoms of the material (this is known as sputtering), while wet etching techniques use a liquid chemical to dissolve the unprotected material and therefore removing it from the chips surface.

As mentioned before dry etching techniques use a plasma to etch the sample. The plasma inside the chamber is created by applying a strong radio-frequency (RF) field to the gas which ionizes the gas molecules. Then by applying a bias voltage to the sample holder and electric field is generated and the ions are accelerated towards the sample. The ions which reach the sample remove the targeted material by sputtering.

To further increase the etching process with plasma, it is possible to add another gas inside the gas chamber. This extra gas will chemically react with the substrate material that is been etched, therefore increasing the etching rate of the substrate material. This etching process, which achieves physical etching (sputtering) and chemical etching, is known as reactive ion etching (RIE).

The direction of the etching process can be classified in two: anisotropic etching and isotropic etching. Isotropic etching acts in all directions of the material, while anisotropic only acts along one direction Fig. 17. If the targeted material was not the only etched during the process, then the etching process is poorly selective. Since the targeted material is the only material that has to be etch, then a highly selectivity etching process is desired Fig. 17. To conclude, a good etching process is highly selective and anisotropic. Thus, it would only etch the desired material and it would create vertical sidewalls for the designed structures (although, depending on the structure been fabricated, sloped walls might be desired).

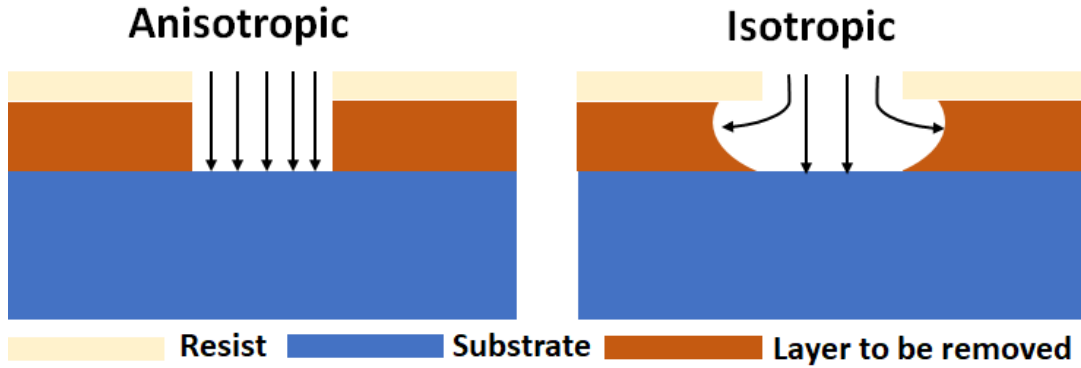


Fig. 16 Difference between anisotropic and isotropic etchings. A perfect anisotropic etching produces vertical walls, while a perfect isotropic etching removes the same amount of the targeted material in all directions.

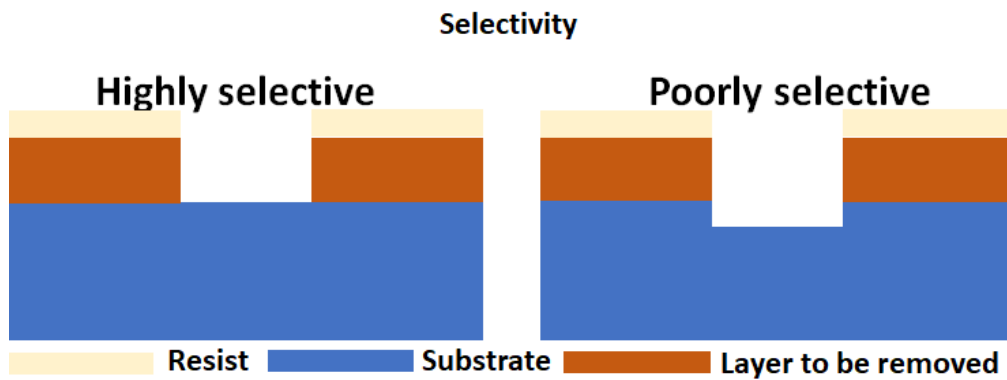


Fig. 17 A highly selective etching process leaves the substrate untouched (left). While a poorly selective etches the targeted layer and part of the substrate (right).

The etching process in this work is based on  $CHF_3$  and  $O_2$ , at a moderate pressure. The RIE etching was carried out in the Oxford Plasmalab 100 unit, and the etching parameters and machine settings are summarized in the next Fig. 18. After the etching, the remaining resist is stripped with an ultrasonic bath with AR 600-71 from Allresist for 5 minutes, followed by 5 minutes of  $O_2$ -ashing in case there are any remaining organics.

$CHF_3/O_2$	38/2 sccm
ICP power	100W
RF power	40W
$Si_3N_4$ etch rate	40 nm / min
Selectivity ( $Si_3N_4/resist$ )	0.9
Temperature	10°C

<b>Carrier wafer</b>	Sapphire
<b>Pressure</b>	12mTorr
<b>Extra</b>	Before loading the sample, a preconditioning of the chamber was done prior the etching by running the same recipe for the length of the etch duration.

Fig. 18 Oxford Plasmalab 100 etching settings and etching parameters.

### 3.6 Design

To be able to follow the deterministic design method of Ref. [11] the structural design shown in Fig. 6 requires some minor modifications: The cavity length has to be zero and the radius of the holes are tapered. By making the cavity length equal to zero the mode volume is minimized and thus the Purcell factor increases, furthermore it reduces the losses from the cavity into the environment [29]. The tapering of the air-holes reduces the losses that originate when total internal reflection criteria is not fulfilled between the interface of the cavity and air-cladding, by providing a smoother confinement of the field at the cavity edges [30].

The cavity parameters are summarized in Fig. 19, where the  $Si_3N_4$  cavity lies on top of a  $SiO_2$  substrate and is covered by a  $hBN$  layer to account for the later introduction of the emitters in an 2-D material heterostructure<sup>4</sup> encapsulated in  $hBN$ . There are  $N$  unit cells on each side of the symmetry line. The width  $w$  was chosen to be the same as the in-line coupled waveguide, which is designed for single mode operation at the targeted resonance frequency of the cavity. The radius is linearly tapered as a function of the hole index. All parameter optimization was done by full 3D FDTD simulation using the software Lumerical.

<sup>4</sup> A heterostructure is vertical stack of 2D materials.

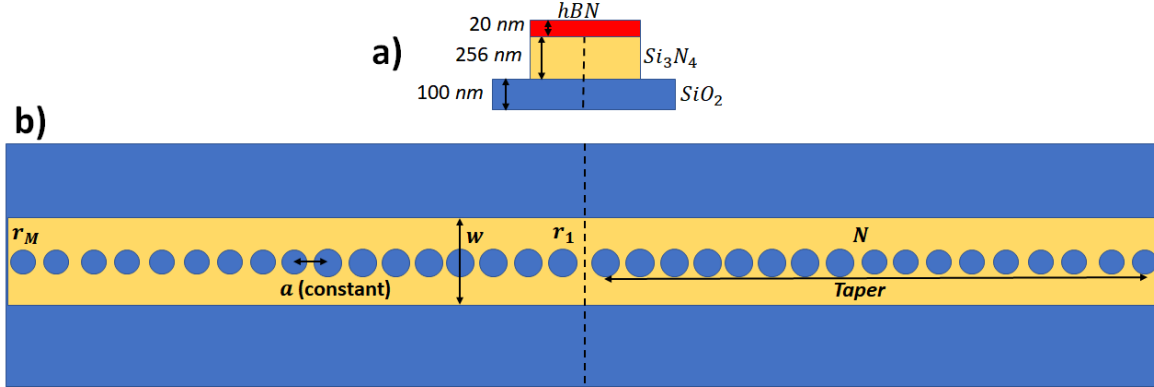


Fig. 19 Cavity design based on Ref. [11]. Schematic of the cavity design parameters. a) Cross-sectional view of the cavity. b) Structure seen from the top without hBN layer.

The design steps from Ref. [11] are summarized as follows:

- 1) A thickness for the nanobeam cavity is chosen, but this is constrained by the available wafers. In this work the thickness of the  $Si_3N_4$  layer from the available wafers is 256 nm.
- 2) A first guess of the periodicity  $a$  can be made from the effective index of the Bloch mode given by  $n_{eff} = \frac{\lambda_0}{2a} \rightarrow a = \frac{\lambda_0}{2n_{eff}}$  where  $\lambda_0$  is the chosen wavelength of the cavity and  $n_{eff}$  can be estimated as the median value of the refractive indices of the three layered materials. The  $a$  value in the design is not vital, because any  $a$  that opens a bandgap can be used as starting point to construct a cavity [29].
- 3) Choose the width  $w$  of the nanobeam cavity. For this work it was constrained to the width of the in-line coupled waveguide designed for single mode operation.
- 4) Find the filling fraction of the first mirror segment that it has its dielectric band-edge at the desired frequency. The filling fraction is given by  $f = \frac{\pi r^2}{a w}$ , where  $r$  is the air hole radius and  $w$  the width of the nanobeam cavity. Since the width is fixed (as mentioned in the previous step) the filling fraction optimization can be performed only as a function of the radius. This is the radius of the first air hole  $r_1$  (the hole closer to the symmetric dashed line). If a value for the radius cannot be found, then the periodicity  $a$  is adjusted accordingly.
- 5) Find the radius  $r_M$  that results in the maximum mirror strength for the desired frequency. The mirror strength is given by:

$$\gamma = \sqrt{\left(\frac{\omega_{air} - \omega_{dielectric}}{\omega_{air} + \omega_{dielectric}}\right)^2 - \left(\frac{\omega_{resonance} - \omega_{mid}}{\omega_{mid}}\right)^2}$$

XXXVII

where  $\omega_{dielectric}$  and  $\omega_{air}$  are the frequencies of the dielectric band and air band respectively,  $\omega_{resonance}$  is the chosen resonance frequency and  $\omega_{mid}$  is the mid-gap frequency.

- 6) Choose the number of mirror segments  $N$  for constructing the mirrors. Having more mirror segments would increase the Q factor but at the expense of having a smaller transmission to the coupled waveguide.
- 7) Create the mirror by tapering the filling fraction quadratically. This is easily achieved by linearly tapering the airhole radius  $r$ , thus leading to quadratic tapering of the filling fraction.

## Chapter 4 Results

Two cavities were fabricated one for a resonance wavelength at 646 nm and the other at 890 nm. In this chapter the simulation results of the design parameters optimization for both wavelengths are first presented, followed by the characterization results of the fabricated cavities.

### 4.1 Simulations

The coupled waveguides chosen to be fabricated with the cavities are ridge-waveguides also known as wire-waveguides, see Fig. 20. Since the thickness of the  $Si_3N_4$  layer from the available wafers is 256 nm the height of the waveguide is constrained to the same height, thus leaving the width as the only free parameter.

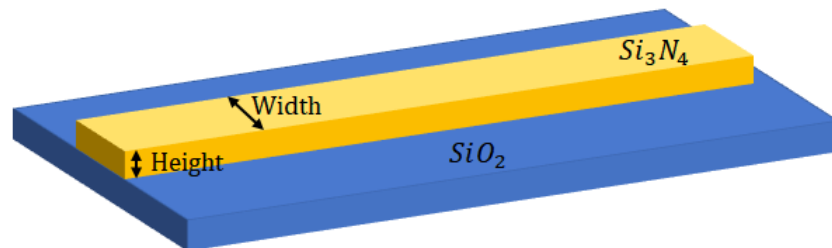


Fig. 20 Schematic of a ridge-waveguide.

The width range for single mode operation of the waveguide, for both wavelengths, was found with Lumerical Mode built in tool. The mode will be guided inside the waveguide when the effective refractive index  $n_{eff}$  of the mode is larger than the cladding: air on the top and  $SiO_2$  at the bottom for this case. If the effective refractive index is larger than  $SiO_2$  index, then it is also larger than the air refractive index, thus the width can be chosen only based on the difference between  $\Delta n = n_{eff\ mode} - n_{eff\ SiO_2}$ . In Fig. 21 the plots of  $\Delta n$  vs waveguide width for both wavelengths are presented.

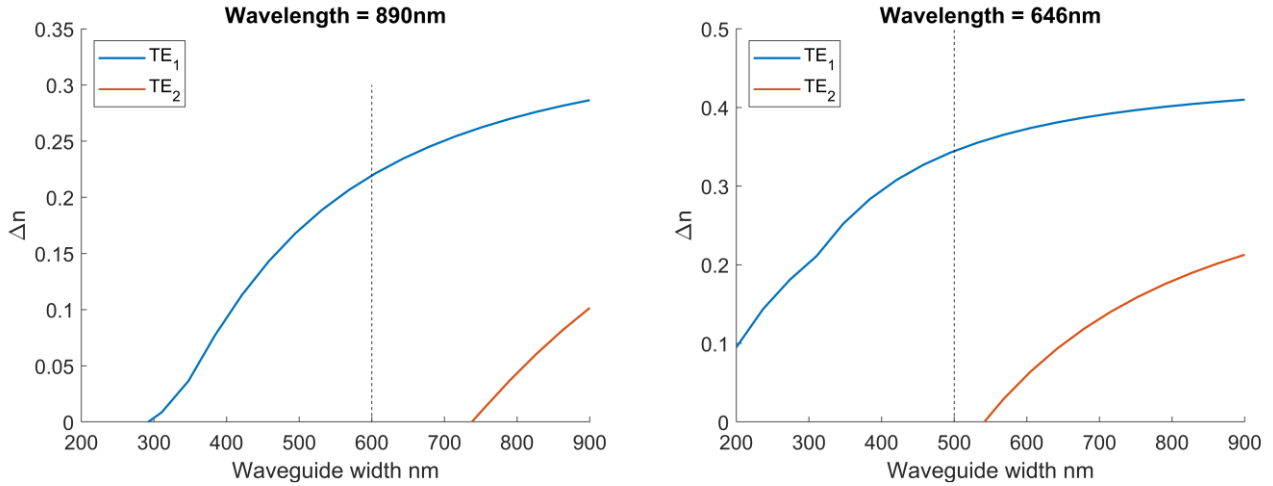


Fig. 21 Width of a ridge waveguide for single mode operation at 646nm and 890nm. The chosen width for fabrication is shown with a dashed line.

In Fig. 21 the plot for the cavity operating at 890 nm is on the left hand side and the one for the cavity operating at 646 nm is on the right hand side. In both plots the change of the  $n_{eff}$  for the first two TE modes (blue for the first one and red for the second) as function of the increasing waveguide width are shown. As the width increases: the refractive index difference  $\Delta n$  increases (thus  $n_{eff}$  also increases), and the waveguide at some point starts supporting another TE mode (if the width is increased more, one would expect that more supported modes would appear). Hence, taking into account that a single mode waveguide is desired, along with a high index difference: the widths chosen for the waveguides operating at 890 nm and 646 nm are 600 nm and 500 nm respectively. With this the design steps 1 and 3, which were introduced at the end of the previous chapter, are covered.

Now, an estimation of the periodicity is made with  $a = \frac{\lambda_0}{2n_{eff}}$ , where  $n_{eff}$  is taken as the effective refractive index felt by the mode at the corresponding waveguide width, yielding for each wavelength:  $n_{eff-890\text{ nm}} \approx 1.7$  and  $n_{eff-646\text{ nm}} \approx 1.8 \rightarrow a_{890\text{ nm}} = 262\text{ nm}$  and  $a_{646\text{ nm}} = 180\text{ nm}$ . If the results obtained with the first guess of the periodicity are not satisfactory,  $a$  can be adjusted. In this work the first guessed did not provided a dielectric band mode with the desired frequency, thus the periodicity was adjusted to  $a_{890\text{ nm}} = 267\text{ nm}$  and  $a_{646\text{ nm}} = 183\text{ nm}$ .

Since  $a$  and the waveguide width are fixed, the radius is the only parameter allowed to vary in the filling fraction equation. Therefore, the dielectric and air bands at the Brillouin zone edge can be obtained as function of radius. This bands can be seen in Fig. 22 were the desired frequencies (890 nm  $\rightarrow$  336.8 THz and 646 nm  $\rightarrow$  466.9 THz) are found at  $r_{1-890 \text{ nm}} = 64 \text{ nm}$  and  $r_{1-646 \text{ nm}} = 62 \text{ nm}$ , which will be the radius of the first air hole in the taper.

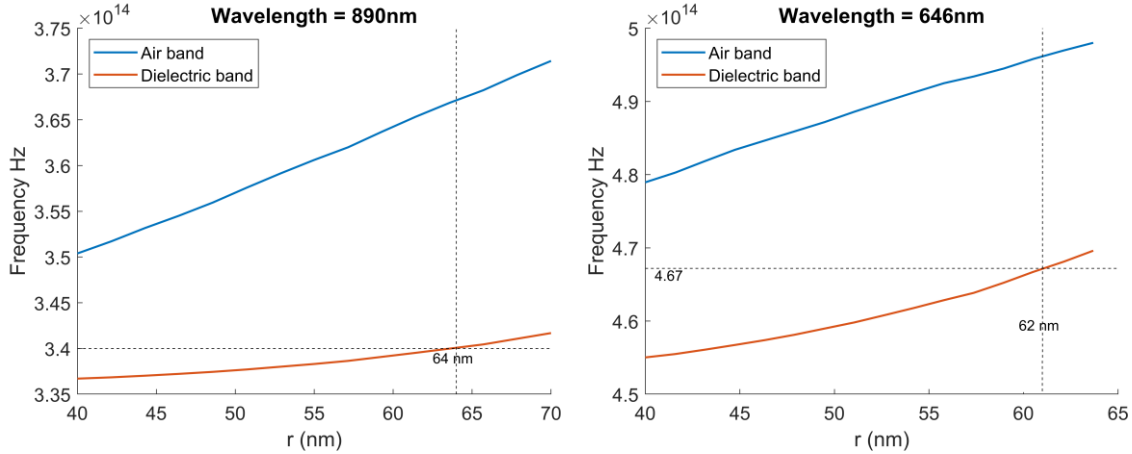


Fig. 22 Dielectric and air bands at the Brillouin zone edge as function of the radius for the cavities operating at 890nm and 646nm.

Next, with the same simulation results from the air and dielectric band and the value of the operating frequency of the cavity, the mirror strength can be computed using the equation XXXVII. Thus, the mirror strength is also optimized as a function of the radius. This allows to find the radius of the last air-hole  $r_M$  for the taper. This radius corresponds to the maximum mirror strength. The mirror strength as function of the radius is shown in Fig 23. Hence, from the data of this plots the corresponding extracted radius with maximum mirror strength are:  $r_{M-890 \text{ nm}} = 44 \text{ nm}$  and  $r_{M-646 \text{ nm}} = 47 \text{ nm}$ .

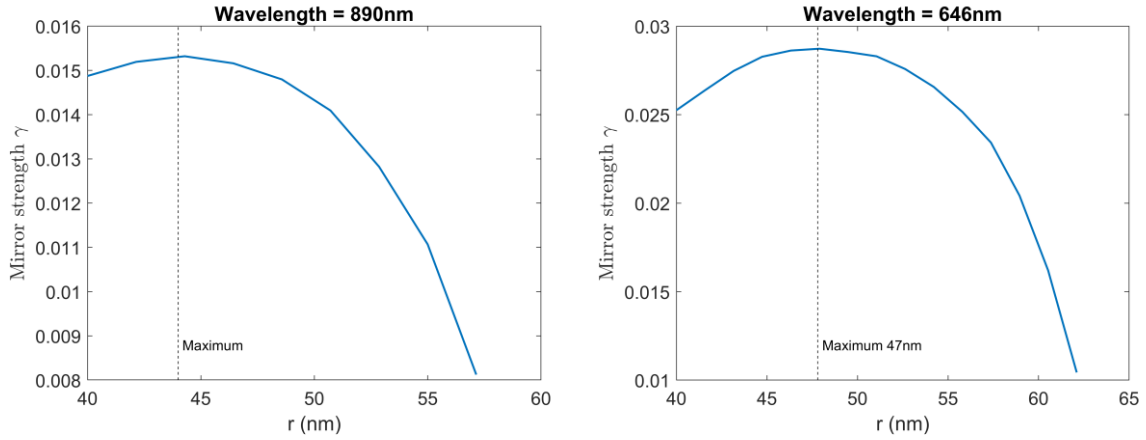


Fig. 23 Mirror Strength as a function of the hole radius for the cavities operating at 890nm (left hand side) and 646nm (right hand side).

Once the values of the radius for the first and last air-holes of the mirror, the taper can be constructed. The shrinking of the air-holes reduces the frequencies of the bands at each unit cell, this results in the confinement of the dielectric mode corresponding to the unit cell with radius  $r_1$ . To ensure this confinement is satisfied, the full bandstructure is plotted for both radius  $r_1$  and  $r_M$ . Fig. 24 shows the dielectric band corresponding to  $r_1$  (colour red) lies inside the bandgap of  $r_M$  (colour blue), thus providing the confinement of the mode.

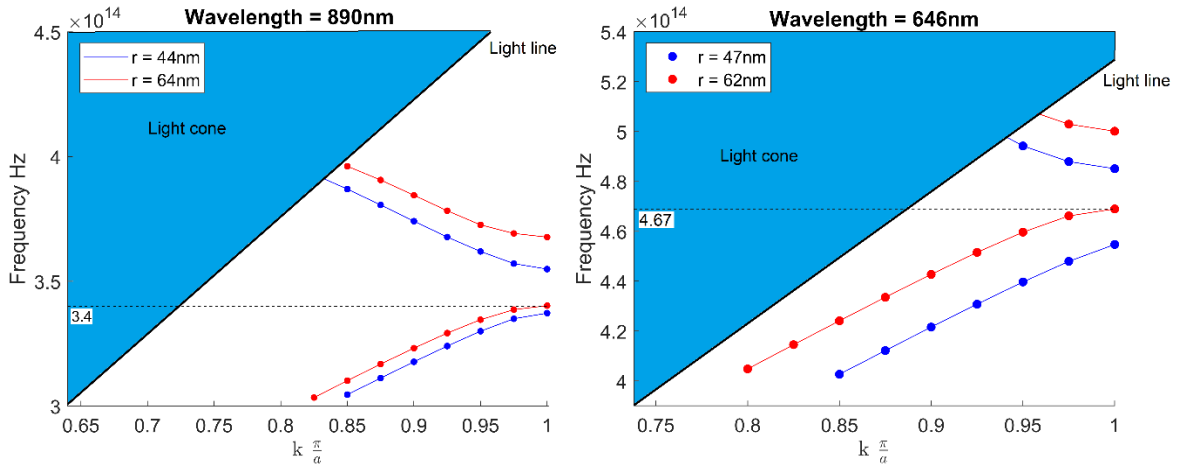


Fig. 24 Full band structure of the air and dielectric bands corresponding to the first (red) and last (blue) radius of the mirror. As required, the dielectric bands of the first  $r_1$  lies inside the bandgap of  $r_M$ . The full band structure for the cavity operating at at 890 nm is shown on the left-hand side and on the right-hand side lies the one corresponding to the cavity operating at at 646 nm.

Finally, the number of mirror segments ( $N$ ) is chosen. Reference [11] recommends at least 15, but if the obtained Q factor is unsatisfactory then  $N$  can be increased. For both cavities  $N$  was chosen equal to 50 segments. Then, with all the design parameters obtained a full 3D simulation of the cavity structure is performed to verify that a Gaussian attenuation of the mode inside the cavity structure is indeed achieved. These results are shown in Fig. 26 and Fig. 27 where the modes profiles are plotted as a function of the distance to the symmetry line of the cavity. In Fig. 26 the mode profile is taken at the middle plane of the cavity (which is located at the middle height, corresponding to  $z=0$ ). While in Fig. 27, to verify that a Gaussian attenuation is indeed achieved, a fit is performed on the field profile corresponding to the central line  $y=0$  of the middle plane  $z=0$ . Table 1 summarizes the optimized parameters obtained from the simulations for both cavities.

<b>Wavelength (<math>\lambda_c</math>)</b>	<b>890 nm</b>	<b>646 nm</b>
<b><math>a</math></b>	267	183
<b><math>r_1</math></b>	64	62
<b><math>r_M</math></b>	44	47
<b><math>w</math></b>	600	500
<b><math>N</math></b>	50	50
<b><math>Q</math></b>	19000	55000
<b><math>V</math></b>	$0.63\left(\frac{\lambda_c}{n_{Si_3N_4}}\right)^3$	$0.94\left(\frac{\lambda_c}{n_{Si_3N_4}}\right)^3$

*Fig. 25 Optimal parameters of the cavities structure.*

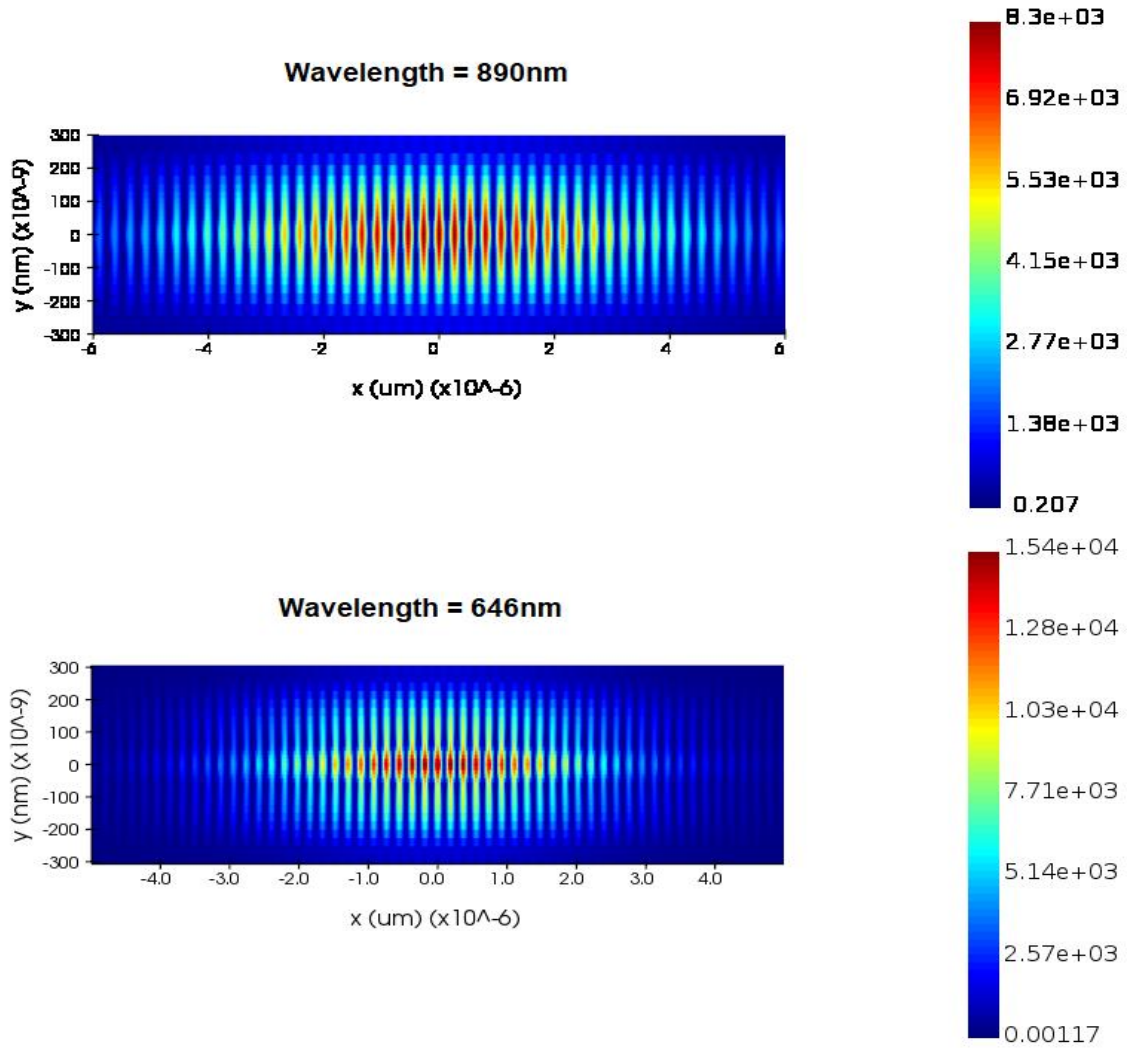


Fig. 26 Mode profiles exhibiting Gaussian attenuation of  $|E|^2$  for both cavities as function of the distance from the symmetry line of the cavity structure (see Fig. 19). The mode profile is taken at the middle plane of the cavity structure corresponding to  $z=0$ .

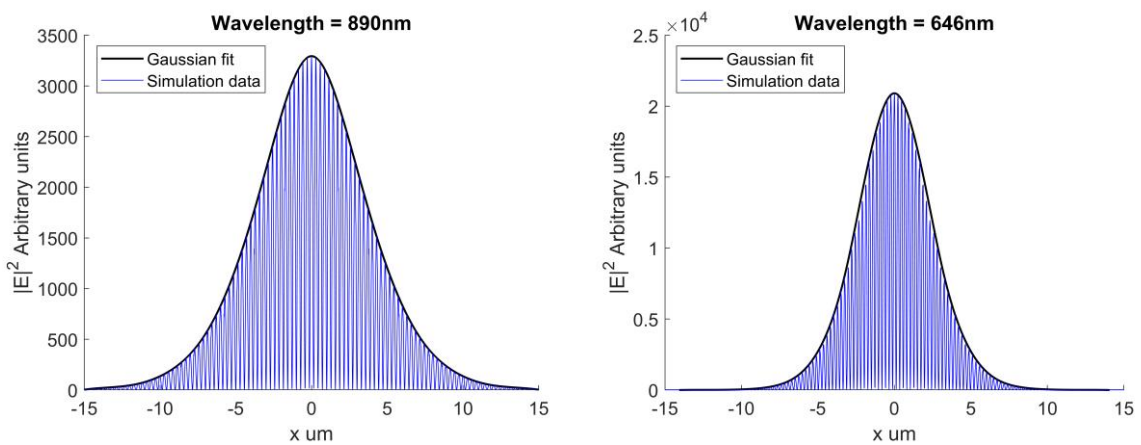


Fig. 27 Mode profiles fitted to a Gaussian Function for both cavities as function of the distance from the symmetry line of the cavity structure. The mode profile is taken at the middle ( $y=0$ ) of the plane which is located at  $z=0$ .

## 4.2 Characterization of the fabricated cavities

To characterize the resonance wavelength of the cavities, room temperature transmission measurements were performed with a continuum laser “YSL sc-pro 7” and a grating spectrometer “Princeton Instruments Acton SpectraPro SP-2750”. The quality factor can be later extracted from these measurements.

The setup shown in Fig. 28 was used to characterize the cavities. The cavities were pumped with the laser using a 100X 0.65 NA objective, and a 3-axis stage allows the focusing of the laser spot into to the cavity input waveguide by adjusting the sample’s position. The cavity response is later collected back through the objective and focused on a beam splitter. The reflected light of the beam splitter is directed to the spectrometer in order to identify the resonant features. The TM mode is suppressed, on the path between the beam splitter and the interferometer, by placing a half-wave plate followed by a linear polarizer. Additionally, on top of the chip, a long distance objective is mounted on a movable stage together with a camera and imaging light, this facilitates the coupling of the laser into the cavity input waveguide and permits the identification of the sample been tested.

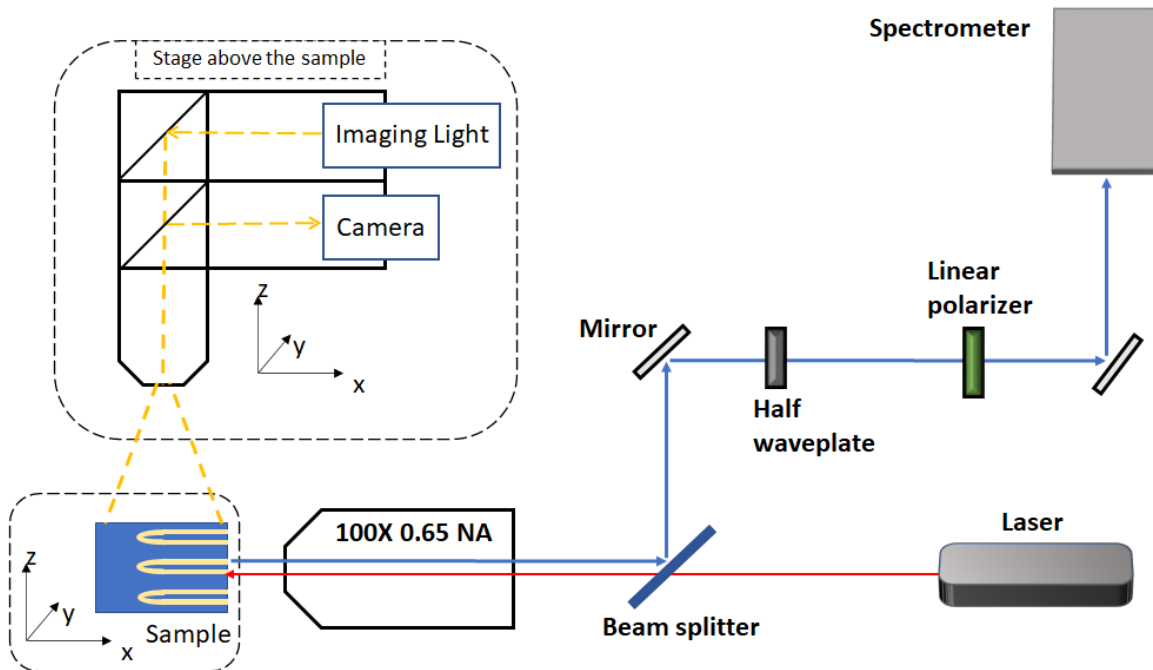


Fig. 28 Room temperature spectroscopy setup.

The spectrometer is equipped with two gratings that ideally provide resolutions of 1200 lines/mm and 150 lines/mm. The lowest resolution grating was first used to locate the resonance peak. Once the peak position was known, the spectrometer was switched to the high-resolution grating in order to perform the measurement and extract the Q factor by fitting the data to a Lorentzian function.

As mentioned in section 1.1.1 if the dielectric configuration is scaled then the frequency of the mode is shifted by the scaling factor of the dielectric configuration. Thus, by multiplying the parameters of a cavity by a scaling factor the resonance frequency of the cavity mode can be tuned. If this property is exploited, then it is possible to overcome any fabrication errors which shift the resonance frequency of the fundamental mode of the cavity from the desired resonance frequency. Therefore, multiple cavities with their parameters modified by a scaling factor, were fabricated on the same chip.

#### **4.2.1 Cavity operating at 646 nm**

For this wavelength cavities were fabricated with scaling from 0.95 to 1.05. Fig. 29 shows an image of some of the fabricated cavities with different scale factors (in color yellow), where the scale factor 1 corresponds to the parameters values found through the simulations results of the previous section. The circle region indicates the location of the cavity, which is the same for each sample. The green arrow indicates the input of the waveguide coupled to the cavity and the red one the output.

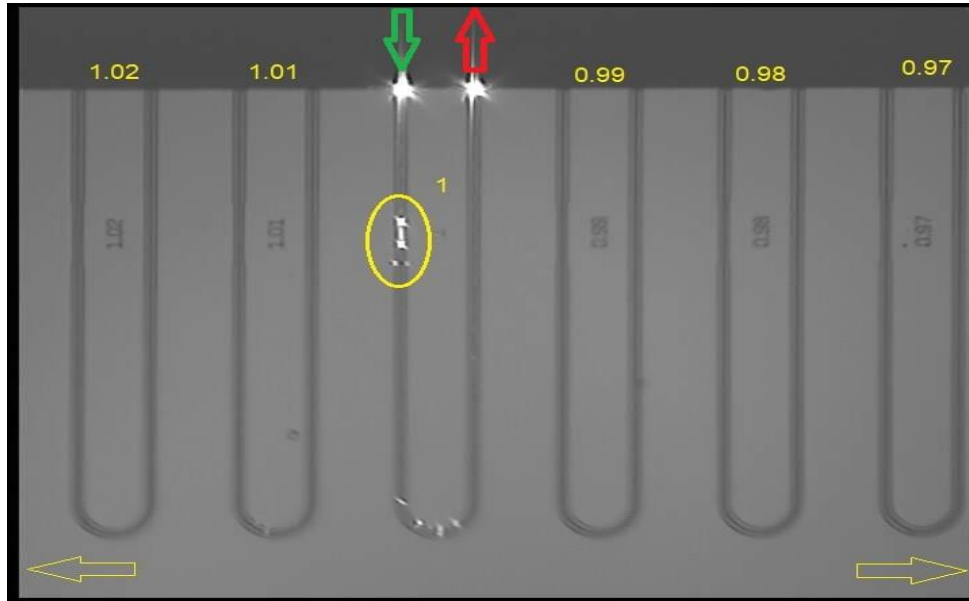


Fig. 29 Fabricate cavities with scaling factor from 0.97-1.02. The green arrows at the bottom indicate the presence of more cavities with different scaling to the sides of the chip. The circle region indicates the location of the cavity.

The transmission spectra of all the cavities is shown in Fig. 30, where the peak with the smallest wavelength corresponds to the fundamental mode of the cavity. The other peaks correspond to higher order cavity modes, but in this work we are not interested in them since the cavity is design to operate with the fundamental mode. More information about this higher order modes can be found in [11] and [29]. A smoothing filter was applied to the data in Fig. 30 making it easier to distinguish the peaks by eye for the reader.

Fig. 31 summarises the wavelength of each peak corresponding to the fundamental mode for each scaled sample. Both the periodicity of the holes  $a$  and their radius  $r$  play a role in defining the resonance of the mode, but the periodicity  $a$  holds a major weight when defining the resonance of the mode, thus a change in the periodicity would cause a larger shift of the resonance than a change in the radius. This is the reason of why the resonance wavelength exhibits a linear growth as a function of the scaling factor. Also, the measurements show that the resonance wavelength for the optimal parameters (scaling factor = 1) is shifted downwards. This is mainly in part due to fabrication imperfections but also considerably due to absence of the hBN layer during the measurements. Further simulations, with the same optimal

parameters (scaling factor =1), shown that the absence of the hBN on top of the cavities causes blueshifting of the resonance wavelength by 10 nm. In other words, the cavity without hBN layer on top operates at a smaller resonance wavelength of 636 nm, which is 10 nm smaller than the resonance wavelength of the cavity with hBN layer on top. From Fig. 31 data shows that none of the fabricated cavities achieves a resonance wavelength at 636 nm. This represents no major issue, since data also shows that every increase of 1% of the scaling factor leads to an increase of the resonance wavelength by 4 nm. Thus, to achieve the resonance wavelength of 636 nm one more scaling of the optimal parameters would be need it: 1.07.

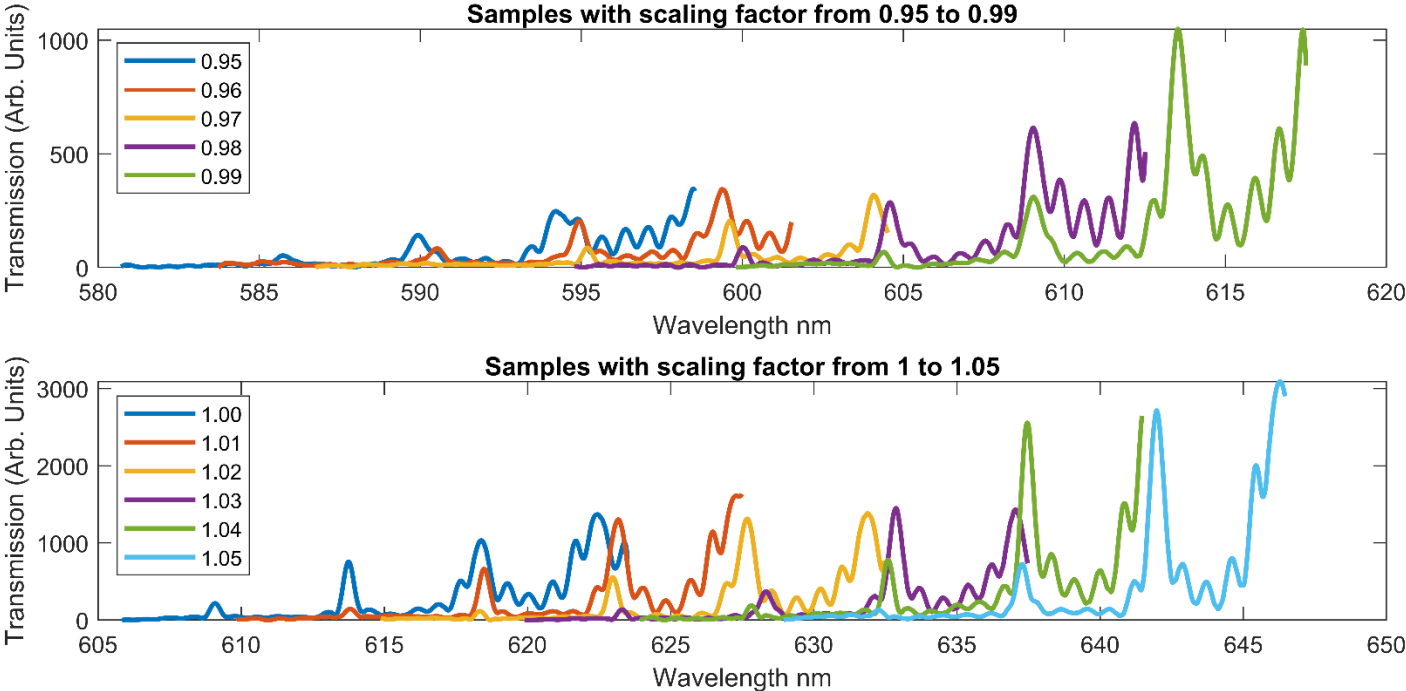


Fig. 30 Transmission spectra from the cavities with scaling factors from 0.95-0.99 on the upper part of the figure and on the lower part the transmission spectra for scaling factors from 1-1.05. The peak with the smallest wavelength is the mode that was designed for the operation of the cavity. A smoothing filter was applied to the data to make easier the distinction of the peaks by eye.

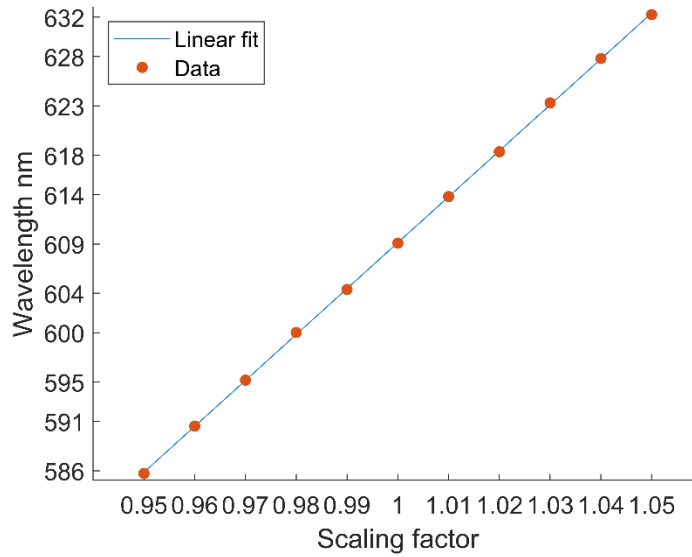


Fig. 31 Resonance wavelength as function of the scaling factor. A linear fit was performed on the data points to show the linear dependence of the resonance wavelength with the scaling factor.

To extract the Q value a Lorentzian fitting is performed on the peak of the fundamental mode. The smallest wavelength peak corresponds to the mode of the cavity for which the cavity is design to operate. The transmission is given Joannopoulos *et al.* in [13].

$$T(\omega) = \frac{\frac{1}{4Q^2}}{\left(\frac{\omega - \omega_0}{\omega_0}\right)^2 - \frac{1}{4Q^2}} \quad \text{XXXVIII}$$

where  $Q$  is the quality factor,  $\omega$  is frequency and  $\omega_0$  is the corresponding frequency to the maximum of the peak. The fabricated devices exhibit Q values in the range from 500 to 3100, where the device with highest  $Q = 3070 \pm 1435$  corresponds to the scaling factor of 1.03. The high uncertainty of this device, when compared to the others, arises from the fact that fewer data points forming the peak where available for the fitting. The Q values obtained for each device are summarized in Fig. 32.

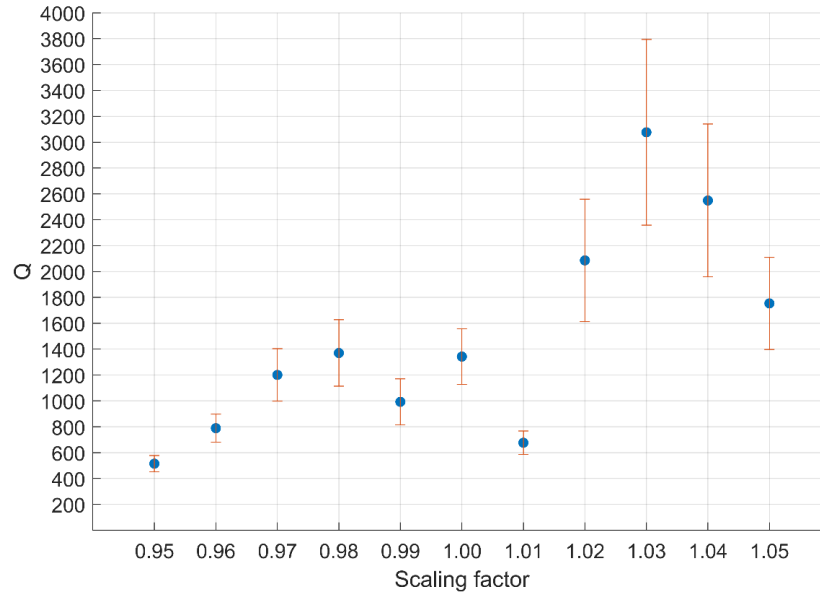


Fig. 32 Q factors with their respective error bar for the different scaling factors.

#### 4.2.2 Cavity operating at 890 nm

For these devices, the coupling was achieved by employing grating couplers on each side of the cavities Fig. 33 (a). Thus, the setup used for characterizing the cavities was slightly modified by removing the camera and imaging light source which were above of the sample, and by adding another beam splitter before the objective Fig. 33 (b) The camera is placed on the new path created by the beam splitter which allows for light imaging of the mounted sample.

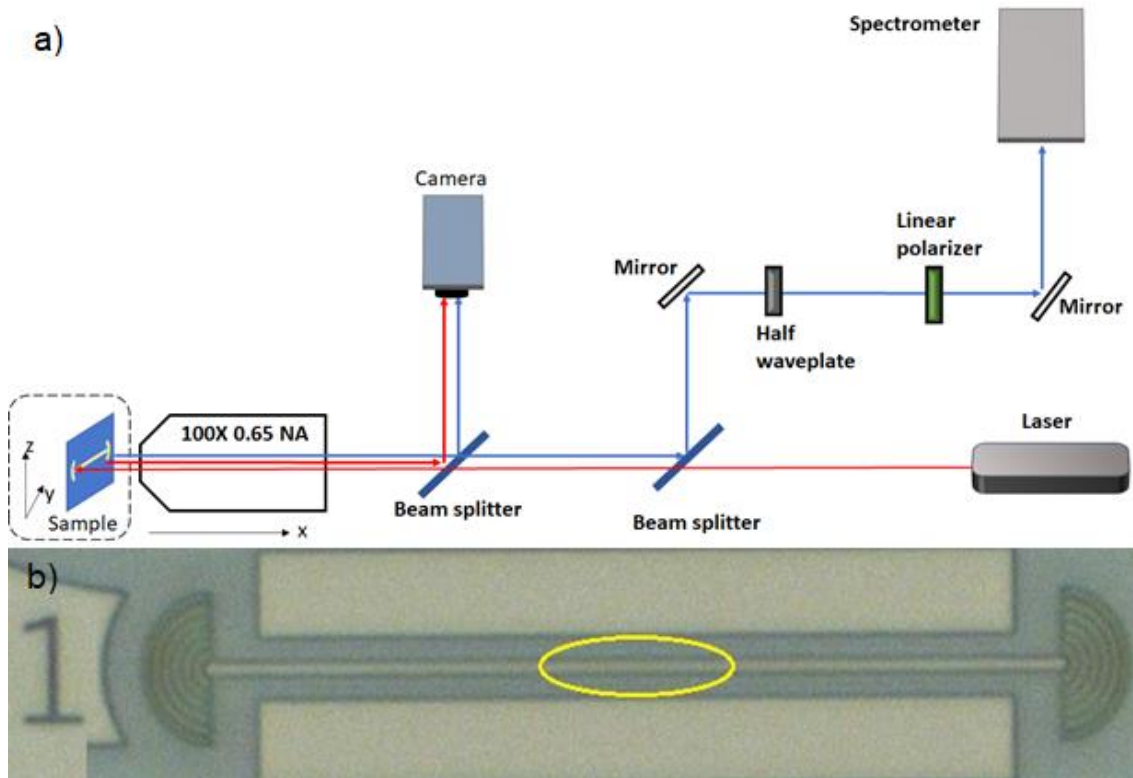


Fig. 33 a) Room temperature spectroscopy setup. b) Photograph of the fabricated device with the optimal parameters of the cavity (scaling factor = 1). The circle region indicates the location of the cavity.

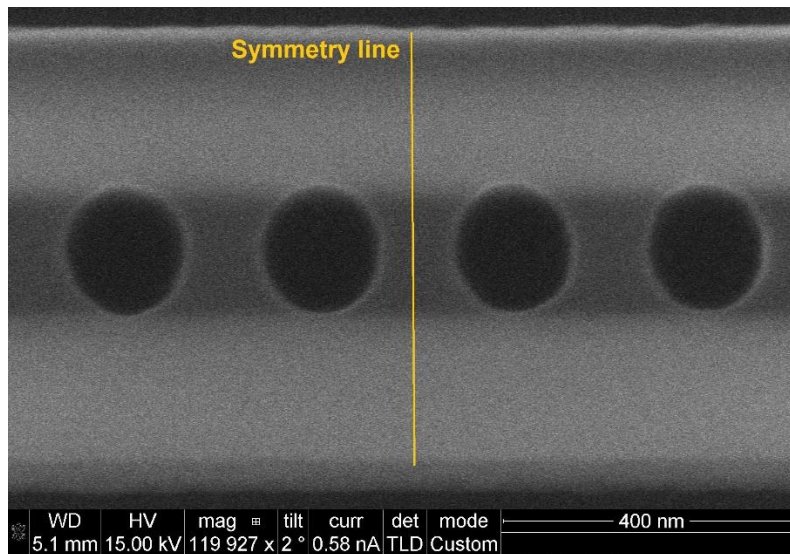


Fig. 34 SEM Image of the cavity operating at 890nm.

These cavities were fabricated with scaling factors ranging from 0.99 to 1.06, and their transmission spectrum exhibited a better signal to noise ratio when compared with the signal to noise ratio of the cavities from Fig. 30. Due to this worse signal to

noise ratio from the cavities from Fig. 30, the fundamental resonance peak of the cavities could not be distinguished from the noise of the signal and consequently a smoothing filter had to be applied to the transmission spectra so the fundamental peak could be distinguished. While, due to the better signal to noise ratio of the cavities from Fig. 35, no smoothing filter was required and the fundamental mode of each device could be distinguished from the noise of the signal.

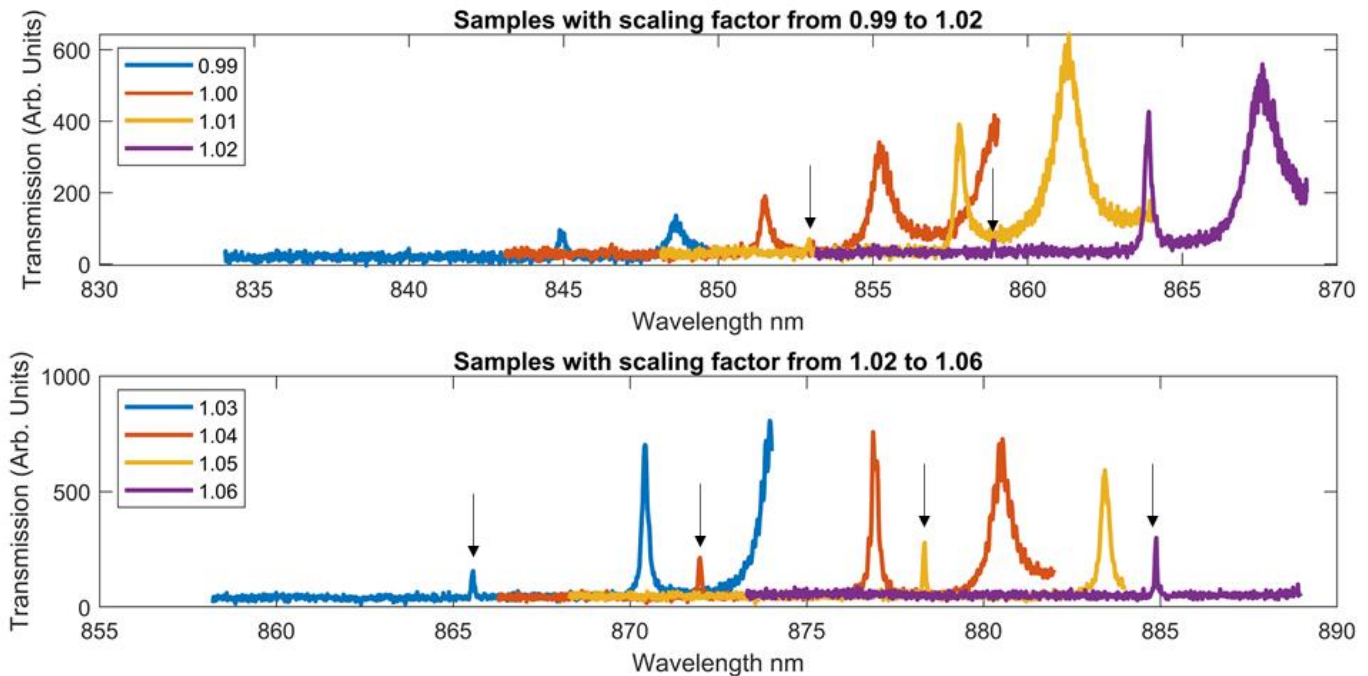


Fig. 35 Transmission spectra from the cavities with scaling factors from 0.99-1.02 on the upper part of the figure and on the lower part the transmission spectra for scaling factors from 1.03-1.06. The black arrows indicate the location of the fundamental mode.

As expected, the resonance wavelength also displays a linear behaviour against the scaling factor, see Fig. 36. The first two cavities with scaling factor 0.99 and 1.00, exhibited a first peak at 845 nm and 852 nm respectively. These peaks at 845 nm and 852 nm can be easily mistaken as the fundamental mode of each cavity. Instead, these peaks at 845 nm and 852 nm correspond to the second mode of each cavity. Like the fundamental modes the second modes are also linearly dependant from the scaling factor. Therefore, to corroborate that the peaks at 845 nm and 852 nm correspond to the second modes, a linear fit was performed on the resonances of the second modes and fundamental modes. The solid line in Fig. 36 shows the linear increase of the resonances of the seconds modes against the scaling factor, while

the dashed line is for the fundamental modes. From the linear fit for the fundamental modes one would expect to find the resonance for the fundamental modes at 841 nm and 847 nm respectively. Also, one might be able to show the presence of the peaks of fundamental modes for the scaling factors 0.99 and 1.00 at their expected wavelength by performing multiple measurements followed by an ensemble averaging on the data, but this was not done because either way their resonances are far from the desired one.

Similar than in the previous section, the simulations without hBN for the optimal parameters shown a downwards shifting of 11 nm for the resonance wavelength. Thus, for these optimal parameters one expects to find the resonance wavelength of the cavity at 879 nm, which is indeed achieved in the device with scaled parameters by 1.05 which shows a resonance wavelength at 878.9 nm.

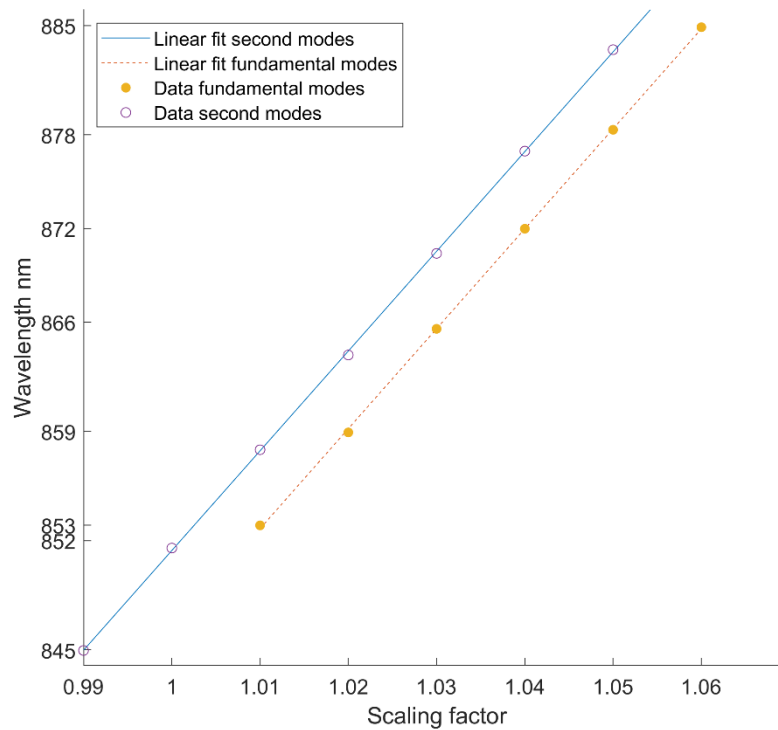


Fig. 36 Resonance wavelength as function of the scaling factor. The solid line corresponds to a linear fit on the second modes of the spectrum for each scaling factor. The dashed line corresponds to a linear fit on the fundamental modes of the spectrum for the scaling factors from 1.01 to 1.06

Same as in the previous section, to extract the Q factor the resonance peak corresponding to the fundamental mode was fitted to the Lorentzian function of XXV.

These devices exhibit Q values in the range from 1600 to 10958 Fig. 37. The device with scaling factor of 1.05 has a resonance wavelength at 878.9 nm and it has a  $Q = 8944 \pm 2823$ .

Since the cavities are designed to operate with the fundamental mode [11, 29] the resonances of 0.99 and 1, which correspond to the second mode of the cavity, have a smaller Q value. While the low Q value of 1.01 and 1.02 is due to the poor transmission of the fundamental mode which is just above the noise baseline.

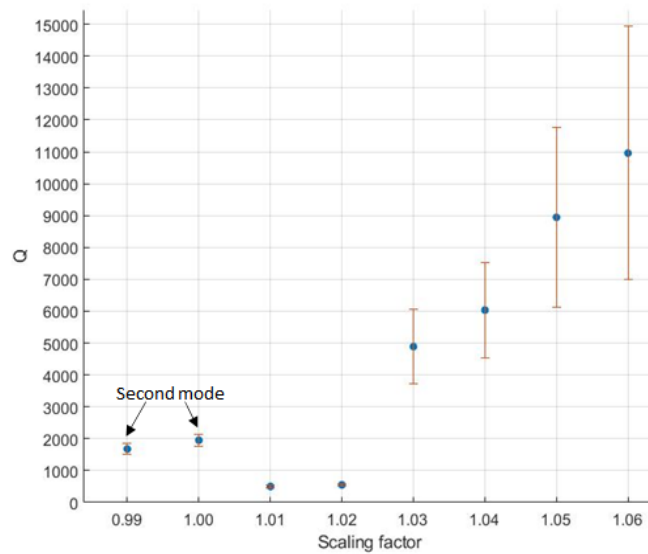


Fig. 37 Q factors with their respective error bar for the different scaling factors. The Q values of the cavities with scaling factors 0.99 and 1.00 are not from the fundamental mode, those values correspond to the Q values of the second mode.

### 4.2.3 Purcell factor and transmission to the coupled waveguide

In reference [29] it is demonstrated that the band edge modes have unity transmission to the coupled waveguide. Thus, their peaks values can be used for estimating the transmission of the fundamental mode to the coupled waveguide.

The peak of the band edge mode is highlighted in the next figure for the cavity with scaling factor 1.04 from the previous section 4.2.2. The transmission yields  $T = 0.28 \pm 0.06$ . Similarly, the transmission for the cavity with scaling factor of 1.05 from section at 4.2.1 is calculated and it yields  $T = 0.09 \pm 0.03$ .

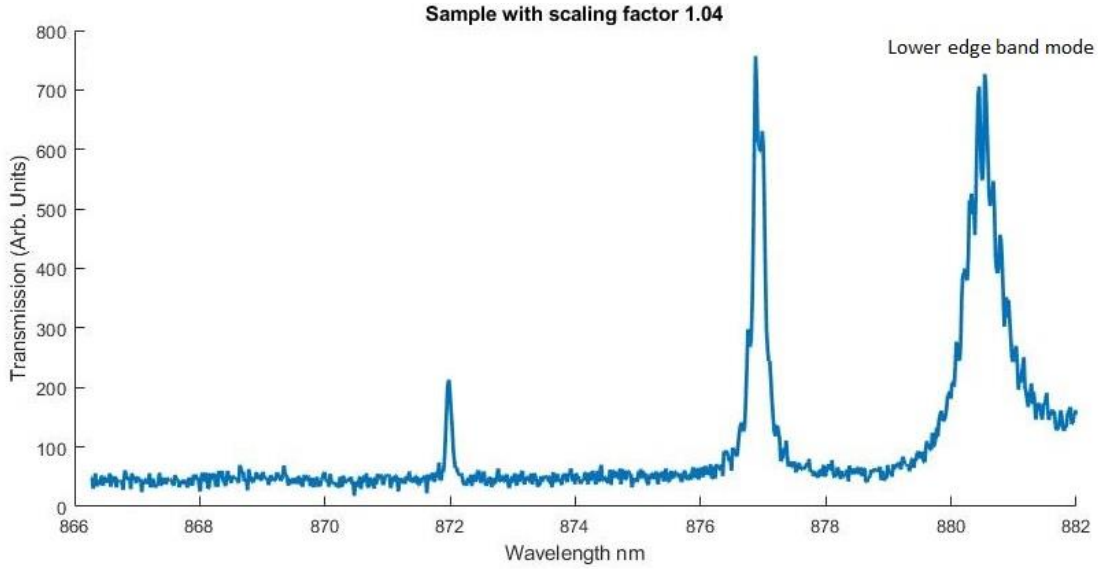


Fig. 38 Transmission spectra for the sample with scaling factor of 1.04 from section 4.2.2.

To conclude this section the Purcell factor is estimated for the cavities 890 nm  $scaling\ factor = 1.05$  and 646 nm  $scaling\ factor = 1.05$ , with the mode volumes obtained from the simulations and measured Q values. For a cavity, whose cavity mode is aligned with the polarization of the emitter, whose linewidth is wider than the emitter's linewidth and whose maxima's location coincides with the position of the emitter, the Purcell factor is given by [31]:

$$F_p = \frac{4}{3\pi^2} \frac{Q}{V} \left(\frac{\lambda}{n}\right)^3 \quad \text{XXXIX}$$

where  $\lambda$  is the resonance wavelength of the cavity,  $n$  the refractive index of the cavity's dielectric,  $Q$  is the quality factor of the cavity and  $V$  is the mode volume. Substituting the previously obtained values in this chapter, equation XXVI yields: for the cavity at 890 nm with scaling factor of 1.05  $F_{p-890\text{ nm}-1.05} = 118 \pm 38$  and for the cavity at 646 nm with scaling factor of 1.05  $F_{p-890\text{ nm}-1.05} = 36 \pm 13$ .

### 4.3 Discussion and further work

The quality factors obtained in the previous section are comparable to the ones previously reported for similar  $Si_3N_4$  cavities: a maximum quality factor of 7000 is

reported in Ref. [18], and values starting from 10000 are reported in Ref. [17]. Still, there is a point to discuss regarding the low Q values of the fabricated cavities for 646 nm (without hBn layer 636 nm) when comparing it to the cavities for 890 nm.

Since the confinement in  $y$  and  $z$  is achieved through total internal reflection, the bandgap of the chosen design does not form a complete bandgap (a complete bandgap exhibits forbidden frequency intervals in any possible direction of light propagation). Because of this, as pointed out in [32], there is always a coupling between modes inside the bandgap (that appear due to the introduction of a defect in the lattice) and the continuum of states located above the light line. This coupling between the modes, for 1-D cavities, can be reduced by localizing the modes in  $k$  space and strongly localizing the mode in real space. The later one can be achieved with a large bandgap and having the resonance mode as close as possible to the mid-gap frequency. While the first one is harder for high mid-gap frequencies since the light cone becomes wider for higher frequencies leading to an increase of the overlapping between the resonance and the continuum of modes. Thus, increasing the leaking of the cavity.

It is possible to further reduce this loss into the continuum by making a suspended cavity [19] [17] [33] (instead of fabricating one on a substrate) which would increase the vertical confinement of the mode. Alternatively, one could try to design a different geometry for the photonic crystal based on momentum space design [34, 35]. But since in this work we are also interested in the Purcell factor for the later integration of the cavities with 2-D emitters (which is the future step of this work), we could also concentrate our efforts in decreasing the mode volume instead of making the quality factor bigger, since the Purcell factor is proportional to  $\frac{Q}{V}$  [31] where  $V$  is the mode volume.

Unfortunately achieving smaller mode volumes than the ones reported here or in [11] would require a change in the design structure (if one wishes to keep the high quality factor values). Since the design used here suffers from a mode volume size increase when adding more segments to the mirror section [11], which is done if one wishes to increase the quality factor.

A remarkable work in this aspect is found in [36] and [37] where they employed a bowtie design for each unit cell. The achieved mode volumes are two orders of magnitude smaller than the ones reported in this thesis and in [11, 29], and with quality factors up to 100000. A similar layout design than the one of this work but with a suspended cavity and rectangular shaped holes is found at [38] with quality factor up to 5000 and mode volumes of one order of magnitude smaller than the ones of this work. Finally, a cavity with low mode volume and high quality factor that employs topological materials for its fabrication can guarantee the existence of a single mode within the photonics bandgap [39].

## Conclusions

In this work, a 1-D deterministic photonic crystal nanocavity design with in-line coupling is reviewed and implemented to fabricate two cavities operating at 646 nm and 890 nm on a  $Si_3N_4$  platform, with transmissions to the coupled waveguide being  $T_{646\text{ nm}} = 0.09 \pm 0.03$  and  $T_{890\text{ nm}} = 0.28 \pm 0.06$ , respectively. This design is advantageous in the sense that the method for computing and optimizing the cavities parameters is not based on trial-and-error, resulting in shorter computation time needed for obtaining the cavity parameters. In the present work the computation time was further reduced by fixing the cavity width at the same width of the coupled waveguide that was designed for single mode operation. In this deterministic design the enhancement of the Q factor for the targeted cavity mode is achieved by tapering the air-holes radius, which leads to spatial localization (in k-space) of the major components at the edge of the Brillouin zone, thus achieving a weak coupling between the mode inside the bandgap and the continuum of states above the light line. However, the cavities achieved with this deterministic design support more than a single mode and these unwanted extra modes cause a further leaking of the light trapped inside the cavity into the environment surrounding the cavity since these extra modes possess a higher coupling to the continuum of states above the light line.

By employing 3D FDTD simulations the cavities were optimized and tested prior to fabrication. It is important to point out that in this design, the periodicity does not have to be a particular value; actually, the cavity parameters can be found for multiple different values of the periodicity  $a$ . Meanwhile, the number of mirror segments  $N$  can play a major role, since it can affect the quality factor  $Q$ , the transmission to the coupled waveguide  $T$ , and the mode volume  $V$  values. A higher number of  $N$  results in a smaller value of  $T$  and in increased values for  $Q$  and  $V$ . A higher value of  $V$  is not desired since it will result in a smaller value for the Purcell factor. Thus, if a cavity with smaller  $V$  and higher  $Q$  is desired a change in the cavity structure will have to be implemented.

Finally using optimized fabrication procedures (spin coating, e-beam lithography and RIE-etching), the designed cavities were experimentally demonstrated to exhibit a high Q value and small mode volume. Thus, these cavities possess the required qualities and potential for the enhancement of the spontaneous emission of single photon emitters that will later be integrated as the next stage of this work.

## References

- [1] E. Yablonovitch, "Photonic Crystals," *Journal of Modern Optics* , vol. 41, no. 2, pp. 173-194, 1994.
- [2] J. D. Joannopoulos, P. R. Villeneuve and S. Fan, "Photonic crystals: putting a new twist on light," *Nature*, p. 143–149, 1997.
- [3] R. M. D. L. Rue and C. Seassal, "Photonic crystal devices: some basics and selected topics," *Laser & Photonics Reviews*, vol. 6, no. 4, p. 564–587, 2012.
- [4] K. J. Vahala, "Optical microcavities," *Nature*, vol. 424, p. 839–846, 2003.
- [5] P. Deotare and M. Loncar, Photonic Crystal Nanobeam Cavities, Dordrecht: In: Bhushan B. (eds) Encyclopedia of Nanotechnology. Springer, 2012.
- [6] F. Peyskens, C. Chakraborty, M. Muneeb, D. V. Thourhout and D. Englund, "Integration of single photon emitters in 2D layered materials with a silicon nitride photonic chip," *Nature communications*, vol. 10, 2019.
- [7] J. L. O'Brien, A. Furusawa and J. Vučković, "Photonic quantum technologies," *Nature photonics*, vol. 3, p. 687–695, 2009.
- [8] D. Psaltis, S. R. Quake and C. Yang, "Developing optofluidic technology through the fusion of microfluidics and optics," *Nature*, vol. 442, p. 381–386, 2006.
- [9] D. V. Thourhout and J. Roels, "Optomechanical device actuation through the optical gradient force," *Nature photonics*, vol. 4, pp. 211-217, 2010.
- [10] M. Eichenfield, J. Chan, R. M. Camacho, K. J. Vahala and O. Painter, "Optomechanical crystals," *Nature*, vol. 462, p. 78–82, 2009.
- [11] Q. Quan and M. Loncar, "Deterministic design of wavelength scale, ultra-high Q photonic crystal nanobeam cavities," *Optics Express*, vol. 19, no. 19, pp. 18529-18542, 2011.
- [12] S. Selim, "Project course report, private communication," 2019.

- [13] J. D. Joannopoulos, S. G. Johnson, J. N. Winn and R. D. Meade, Photonic crystals molding the flow of light, Princeton, New Jersey: Princeton University Press, 2008.
- [14] Simulator, 3D Electromagnetic Lumerical Inc.  
<https://www.lumerical.com/products/>. [Online].
- [15] S. D. Gedney, Introduction to the Finite-Difference Time-Domain (FDTD) Method for Electromagnetics, University of Kentucky: Morgan & Claypool, 2011.
- [16] J.-P. Bérenger, Perfectly Matched Layer (PML) for Computational Electromagnetics, Centre d'Analyse de Défense Arcueil, France: Morgan & Claypool, 2007.
- [17] M. Khan, T. Babinec, M. W. McCutcheon, P. Deotare and M. Lončar, "Fabrication and characterization of high-quality-factor silicon nitride nanobeam cavities," *Optics Letters*, vol. 36, no. 3, pp. 421-423, 2011.
- [18] T. K. Fryett, Y. Chen, J. Whitehead, Z. M. Peycke, X. Xu and A. Majumdar, "Encapsulated Silicon Nitride Nanobeam Cavity for Hybrid Nanophotonics," *ACS Photonics*, vol. 5, no. 6, p. 2176–2181, 2018.
- [19] P. B. Deotare, M. W. McCutcheon, I. W. Frank, M. Khan and M. Loncar, "High quality factor photonic crystal nanobeam cavities," *Appl. Phys. Lett.*, vol. 94, p. 121106, 2009.
- [20] M. W. McCutcheon and M. Loncar, "Design of a silicon nitride photonic crystal nanocavity with a Quality factor of one million for coupling to a diamond nanocrystal," *Optics Express*, vol. 16, no. 23, pp. 19136-19145, 2008.
- [21] D. J. Blumenthal, R. Heideman, D. Geuzebroek and A. Leinse, "Silicon Nitride in Silicon Photonics," *Proceedings of the IEEE*, vol. 106, no. 12, pp. 2209 - 2231, 2018.
- [22] R. Baets, A. Z. Subramanian, S. Clemmen, B. Kuyken, P. Bienstman, N. L. Thomas, G. Roelkens, D. V. Thourhout, P. Helin and S. Severi, "Silicon Photonics: silicon nitride versus silicon-on-insulator," in *Optical Fiber Communications Conference and Exhibition*, 2016.

- [23] S. Samal, S. Mohanty and S. K. Nayak, *Superhydrophobic Polymer Coatings: Fundamentals, Design, Fabrication, and Applications*, 1st ed., Amsterdam, Netherlands: Elsevier, 2019.
- [24] M. Tyona, "A theoretical study on spin coating technique," *Advances in Materials Research*, Vols. 2, No. 4, pp. 195-208, 2013.
- [25] Allresist, "Positive E-Beam Resists AR-P 6200," *CSAR 62 datasheet*, 2014.
- [26] M. Totzeck, W. Ulrich, A. Göhnermeier and W. Kaiser, "Pushing deep ultraviolet lithography to its limits," *Nature photonics*, vol. 1, p. 629–631, 2007.
- [27] V. R. Manfrinato, L. Zhang, D. Su, H. Duan, R. G. Hobbs, E. A. Stach and K. K. Berggren, "Resolution Limits of Electron-Beam Lithography toward the Atomic Scale," *Nano Letters*, vol. 13, no. 4, p. 1555–1558, 2013.
- [28] "The Raith\_GDSII MATLAB toolbox was developed at the National Institute for Nanotechnology and is maintained at the University of Alberta nanoFAB Centre; it is available at [github.com/nrc-cnrc/Raith\\_GDSII](https://github.com/nrc-cnrc/Raith_GDSII)."
- [29] Q. Quan, P. B. Deotare and M. Loncar, "Photonic crystal nanobeam cavity strongly coupled to the feeding waveguide," *Applied Physics Letters*, vol. 96, no. 203102, 2010.
- [30] Y. Akahane, T. Asano, B.-S. Song and S. Noda, "High-Q photonic nanocavity in a two-dimensional photonic crystal," *Nature*, vol. 425, pp. 944-947, 2003.
- [31] M. Pelton, "Modified spontaneous emission in nanophotonic structures," *Nature photonics*, vol. 9, pp. 427-435, 2015.
- [32] S. Fan, J. N. Winn, A. Devenyi, J. C. Chen, R. D. Meade and J. D. Joannopoulos, "Guided and defect modes in periodic dielectric waveguides," *Journal of the Optical Society of America B*, vol. 12, no. 7, pp. 1267-1272, 1995.
- [33] A. Loukas, C. Aristi, G. Georgios, B. Eftychia, P. George, S. Maria-Christina, R. Ioannis and P. Nikolaos, "Design and fabrication of suspended Si<sub>3</sub>N<sub>4</sub> nanobeam cavities," *Microelectronic Engineering*, vol. 159, pp. 42-45, 2016.

- [34] K. Srinivasan and O. Painter, "Momentum space design of high-Q photonic," *Optics Express*, vol. 10, no. 15, pp. 670-684, 2002.
- [35] D. M. Atkin, P. S. J. Russell, T. A. Birks and P. J. Roberts, "Photonic band structure of guided bloch modes in high index films fully etched through with periodic microstructure," *Journal of Modern Optics*, pp. 1035-1053, 2009.
- [36] S. Hu and S. M. Weiss, "Design of Photonic Crystal Cavities for Extreme Light Concentration," *ACS Photonics*, vol. 3, no. 9, p. 1647–1653, 2016.
- [37] S. Hu, M. Khater, R. Salas-Montiel, E. Kratschmer, S. Engelmann, W. M. J. Green and S. M. Weiss, "Experimental realization of deep-subwavelengthconfinement in dielectric optical resonators," *Science Advances*, vol. 4, no. 8, 2018.
- [38] R. Miura, S. Imamura, R. Ohta, A. Ishii, X. Liu, T. Shimada, S. Iwamoto, Y. Arakawa and Y. K. Kato, "Ultralow mode-volume photonic crystal nanobeam cavities for high-efficiency coupling to individual carbon nanotube emitters," *Nature Communications*, vol. 5, no. 5580, 2014.
- [39] Y. Ota, R. Katsumi, K. Watanabe, S. Iwamoto and Y. Arakawa, "Topological photonic crystal nanocavity laser," *Communications Physics*, no. 86, 2018.
- [40] M. Grande, G. Calo, V. Petruzzelli and A. D'Orazio, "High-Q Photonic crystal nanobeam cavity based on a silicon Nitride membrane incorporating fabrication imperfections and a low-index material layer," *Progress In Electromagnetics Research B*, vol. 37, pp. 191-204, 2012.
- [41] P. Lalanne and J. P. Hugonin, "Bloch-Wave Engineering for High-Q, Small-V Microcavities," *Journal of Quantum Electronics*, vol. 39, no. 11, 2003.
- [42] D. Englund, I. Fushman and J. Vuckovic, "General recipe for designing photonic crystal cavities," *Optics Express*, vol. 13, no. 16, pp. 5961-5975, 2005.
- [43] T. Liu, H. Qiu, T. Yin, C. Huang, G. Liang, B. Qiang, Y. Shen, H. Liang, Y. Zhang, H. Wang, Z. Shen, D. W. Hewak and Q. J. Wang, "Enhanced light-matter interaction in atomically thin MoS<sub>2</sub> coupled with 1D photonic crystal nanocavity," *Optics Express*, vol. 25, no. 13, pp. 14691-14696, 2017.

- [44] J. Vučković, M. Pelton, A. Scherer and Y. Yamamoto, "Optimization of three-dimensional micropost microcavities for cavity quantum electrodynamics," *Physical Review A*, vol. 66, no. 2, 2002.
- [45] M. Stepanova and S. Dew, *Nanofabrication Techniques and Principles*, New York: Springer, 2012.